ELSEVIER

Contents lists available at ScienceDirect

Acta Materialia

journal homepage: www.elsevier.com/locate/actamat



Full length article



Extraordinary creep resistance in a non-equiatomic high-entropy alloy from the optimum solid-solution strengthening and stress-assisted precipitation process*

Shuying Chen ^{a,*}, Jingbo Qiao ^a, Haoyan Diao ^b, Tengfei Yang ^c, Jonathan Poplawsky ^d, Weidong Li ^b, Fanchao Meng ^a, Yang Tong ^a, Liang Jiang ^a, Peter K. Liaw ^{b,*}, Yanfei Gao ^{b,*}

- ^a Institute for Advanced Studies in Precision Materials, Yantai University, Yantai 264005, China
- ^b Department of Materials Science and Engineering, The University of Tennessee, Knoxville, TN 37996, USA
- ^c College of Materials Science and Engineering, Hunan University, Changsha 410082, China
- ^d Center for Nanophases Materials Sciences, Oak Ridge National Laboratory, Oak Ridge, TN 37831, USA

ARTICLE INFO

ABSTRACT

Keywords: High-entropy alloy Creep resistance Stress-assisted precipitation process Improving creep resistance has commonly been achieved by the optimization of alloy design that results into strong solid-solution strengthening and/or coherent precipitates for dislocation blockage. High-entropy alloys (HEAs), despite their single-phase solid-solution nature, only exhibit creep properties that are comparable to precipitate-strengthened ferritic alloys. Moreover, many HEAs are found to be plagued with many incoherent second phases after long-term annealing, which reduces the lifetime and thus prohibits their usage at elevated temperatures. The present work demonstrates the extraordinary creep resistance of a non-equiatomic Al_{0.3}CoCrFeNi HEA, in which the creep strain rate is found to be several orders of magnitude lower than the Cantor alloy and its subsets. Using a suite of characterization tools such as atom probe tomography (APT) and transmission electron microscopy (TEM), it was shown that a B2 precipitate phase that has been widely seen during annealing is suppressed during the early stage of the creep deformation. Currently, metastable and coherent L12 precipitates emerge and provide significant creep strengthening. This observation is rationalized by the coupling between the applied stress and the lattice mismatch. In the range of 973 \sim 1033 K, the stress exponent and activation energy were determined to be 3-6.53 and 390-548.2 kJ mol⁻¹, respectively. The creep lifetime, on the other hand, is comparable to Cantor subset alloys because the precipitate free zone near the grain boundaries does not provide sufficient constraint for the grain boundary cavity growth. The present work provides a pathway to design novel HEAs with improved creep resistance.

1. Introduction

For environmental and economic considerations, thermal power plants are constantly challenged to improve operational efficiency and reduce greenhouse gas emissions. The efficiency of the conventional fossil power plant is critically dependent on the steam temperature and pressure. By increasing the steam temperature from 866 to 973 K, the efficiency can increase from 47%, i.e., the typical efficiency of current

state-of-the-art plants, to 55% [1]. However, such improvements cannot be achieved without the advancement of structural materials capabilities. The boilers, steam turbines, and gas turbines made of commercial ferritic steel can only be operated at temperatures below 893 K due to their limited creep resistance at higher temperatures [1]. Thus, new alloys need to be developed to enable higher operating temperatures in order to improve the thermal efficiency of thermal power plants.

Recently receiving much attention, investigating new high entropy

E-mail addresses: sychen@ytu.edu.cn (S. Chen), pliaw@utk.edu (P.K. Liaw), ygao7@utk.edu (Y. Gao).

^{*} This manuscript has been authored by UT-Battelle, LLC under Contract No. DE-AC05–000R22725 with the U.S. Department of Energy. The United States Government retains and the publisher, by accepting the article for publication, acknowledges that the United States Government retains a non-exclusive, paid-up, irrevocable, world-wide license to publish or reproduce the published form of this manuscript, or allow others to do so, for United States Government purposes. The Department of Energy will provide public access to these results of federally sponsored research in accordance with the DOE Public Access Plan (http://energy.gov/downloads/doe-public-access-plan).

^{*} Corresponding authors.

alloys (HEAs) has been considered as a potential strategy due to promising properties in extreme environments [2–7], such as remarkable high-temperature strengths (even superior to some superalloys) and great resistance to irradiation and oxidation [8–12]. The large compositional tunability brings opportunities for developing advanced alloys with an outstanding combination of different properties [13–17]. Meanwhile, the endless composition pool brings a new challenge of designing HEAs with targeted properties. From some previous studies, the HEAs with FCC structure are suggested to be the most potential candidates for creep resistant alloy design due to their low cost, superior oxidation and corrosion resistance, tunable microstructure, and strength at elevated temperatures, compared with that of BCC structure [10–17]. Thus, the HEAs with FCC structure will be focused on and systematically investigated in the present work.

Recently, most studies of creep behavior are conducted on the Cantor alloy, CoCrFeMnNi and its subset (e.g., CoCrNi and CoCrFeNi), or its derivatives such as Al_xCoCrFeMnNi. They demonstrate outstanding creep properties and stability, compared with conventional alloys, e.g., 304 stainless steel (SS) and some commercial ferritic steels (P92, P122, T91, and FBB8) [18]. The earliest study of creep deformation was conducted by Woo et al. [19], in which the creep deformation was investigated by the in situ neutron diffraction in the CoCrFeMnNi HEA in the temperature range of 800-1000 K. They found that the dominant deformation mode is the dislocation glide at 800 K and diffusion-controlled dislocation creep at 1000 K, respectively. Kang et al. [20] studied creep properties and fracture behavior of the CoCrFeMnNi HEA at temperatures of 873 and 923 K, which was dominated by a glide-controlled mode. Further tensile creep tests of the CoCrFeNiMn HEA were performed over a temperature range (773-1173 K), the creep rate is believed to be dominated by the dislocation-dislocation interaction and dislocation climb [21-24]. Owing to the local atomic environment inhomogeneity especially exacerbated by chemical short-range order and lattice distortion, dislocation in the high entropy alloy matrix experiences a rugged atomic and energy landscape, contributing to a strengthening beyond the conventional solution strengthening effect in the alloys with the one-principal element. Thus, the dislocation substructure formed during the creep process underlined the predominance of the interaction between moving dislocation and rugged landscape generated by local environment inhomogeneity in the concentrated solid solution matrix at elevated temperatures [22]. Moreover, it is proposed that the concentration of alloying elements in the high entropy matrix is inherently non-uniform. Even a weak but complex element-element interaction can result in a remarkable influence on the deformation behavior [25]. In order to improve the creep strength of single-phase FCC HEAs, solid solution hardening and precipitation strengthening were adopted by adding an element with a large radius. For instance, Dobes et al. [26] reported a strategy to enhance the creep properties by introducing oxide particles in CoCrFeMnNi matrix. The oxide-dispersion-strengthened alloy presented a lower creep strain rate of 10^{-9} /s under 30 MPa and 973 K, which was due to the induced effective stress by the presence of oxides. Kim et al. [27] reported the creep behavior in the cast $Al_{0.5}$ CoCrFeMnNi alloy with a minor BCC phase. They suggested that the creep properties at high temperatures are enhanced by the addition of Al atoms that lead to both solid solution hardening and precipitation strengthening. Additionally, another way to improve the creep strength is lowering the stacking fault energy by adjusting the constituents of Cantor alloy. For example, CoCrNi and CoCrFeNi as a subset of CoCrFeMnNi were also studied in the range of 923-1073 K. Resulting from the enhanced solid-solution strengthening and lower stacking fault energy, CoCrNi alloy presented a longer creep rupture life and lower steady-state creep rate than CoCrFeMnNi [18,28]. The precipitate formed during the creep experiment in Cantor, CoCr-FeNi, or CoCrNi is rarely observed because of the extremely low density of precipitates [18,22,23], resulting in a negligible contribution to the creep resistance. These prior studies demonstrate some potentials of HEAs for high temperature applications, but an extensive understanding

of the precipitate effect on the deformation mechanism and creep resistance in HEAs is still desperately desired.

Another promising alloy design approach is to replace Mn with Al in the Cantor alloy, resulting in Al_{0.3}CoCrFeNi alloys that can achieve a superior tensile strength of 1.8 GPa by obtaining multiple combinations of hierarchical multi-phase microstructures [17], which might serve as a potential candidate for the elevated-temperature application. Therefore, it is speculated that the single phase of FCC solid solution in Al_{0.3}CoCrFeNi may generate a large number of precipitates during long-term creep tests, which have a significant effect on the deformation mechanism and creep properties and enhance the creep strength. Precipitates in Cantor and subset alloys can be detrimental but the addition of Al provides vast opportunities to produce Ni-Al precipitates. Only one creep study of Al_{0.3}CoCrFeNi was performed at high temperatures by the compression creep tests. They observed the dislocation-precipitate interaction in the crept specimen [29], but their study is limited in the stress/temperature range and also lacks comprehensive characterizations. Important questions such as how precipitates appear and grow remain elusive.

A systematic understanding of microstructural evolution and deformation mechanism of the ${\rm Al_{0.3}CoCrFeNi}$ alloy under tensile creep is still not clear, which may obscure its capability as components in fossil energy power plants with a steam temperature of 973 K or higher. It was found that the single phase of FCC ${\rm Al_{0.3}CoCrFeNi}$ alloy is not stable at the intermediate temperature and will decompose into various precipitates. Such phase instability may cause the dislocation/particle interaction during the creep test, which will have an important effect on the creep deformation mechanism and then creep behaviors. In addition, we aim to find out a potential candidate with excellent creep resistance for the elevated-temperature application of fossil energy power plants. Further alloying of this material may change the compositions of these precipitates and therefore tune the lattice mismatch. At the same time, the present study could deepen our fundamental understanding of the creep deformation mechanisms of HEAs at elevated temperatures.

2. Experimental procedure

The nominal chemical composition of the Al $_{0.3}$ CoCrFeNi is 7.00Al-23.26Co-23.26Cr-23.26Fe-23.26Ni [atomic percentage (at%)]. An ingot with a dimension of $127 \times 305 \times 19 \text{ mm}^3$ was fabricated by Sophisticated Alloys, Inc., using the vacuum-induction-melting facility. Then the specimen underwent a hot-isostatic-pressing (HIP) process (1477 K and 103 MPa) for 4 h in order to reduce defects formed during the casting and cooling processes.

The uniaxial tension experiment was performed on $Al_{0.3}$ CoCrFeNi, with a computer-controlled Material Test System (MTS) servohydraulictesting machine. The flat dog-bone tension samples with a gage length of 10 mm were machined by Electrical Discharge Machining (EDM). The tension test was carried out at an engineering strain rate of 2×10^{-4} /s.

The tension creep behavior of the $Al_{0.3}$ CoCrFeNi HEAs was conducted under the constant load mode, covering the stress range of 50 \sim 120 MPa and the temperature range of 823 \sim 1033 K, with a round-type sample (a gage diameter of 3.175 mm and a gage length of 28 mm). A thermocouple was attached to the center of the specimen gage-length section. The sample was heated to and held at a target temperature for at least 1 h until the sample temperature was stabilized within \pm 1 $^{\circ}$ C.

The microstructure and fractography of crept samples were investigated by scanning electron microscopy (SEM) using a Tescan Amber equipped with energy dispersive spectroscopy (EDS) and an electron back-scattering diffraction (EBSD; EDAX, Oxford). Specimens prepared for EBSD analysis were ground using SiC paper, followed by Vibratory Polisher (VibroMet 2, Buehler). The step size of EBSD scanning was 0.1 μm . The EBSD data was processed using Crystal analysis software. Transmission electron microscopy (TEM) observations were performed, using a 300 keV Tecnai F30 microscope. The TEM samples were prepared by mechanical polishing to approximately 30 μm in thickness,

followed by ion milling at an ion energy of $\sim 2\,kV$ and an incident angle of \pm 6 °. Atom probe tomography (APT) specimens were extracted using a common liftout and sharpening techniques using a Si micropost array using a Thermo Fisher Nova 200 dual beam focused ion beam/SEM (FIB/SEM) [30]. The APT experiments were performed at Oak Ridge National Laboratory, using a CAMECA local electrode atom probe (LEAP) 4000X HR in laser mode with a 30 K base temperature and a 60 pJ laser power. At least 5 million ions were collected for each sample to ensure adequate data statistics. The datasets were reconstructed and analyzed, using CAMECA's IVAS software [31].

3. Results

3.1. Microstructure and properties before creep

The initial microstructure before the creep tests is displayed in Fig. 1. Equiaxed grains with a grain size of about 303 μm were observed in Fig. 1(a), with a single FCC phase occurring in Fig. 1(b). APT maps of the five constituent elements are shown to be distributed randomly in the matrix (Fig. 1(c)), which is consistent with the previous studies that a single FCC phase formed at temperatures above 1373 K [32]. Additionally, the tensile experiment of Al $_{0.3}$ CoCrFeNi was performed at room temperature, and the corresponding representative engineering stress-strain curve was presented in Fig. 2. The investigated sample showed a noticeable work hardening after the yield point, with a yield stress of 210 MPa, peak stress of 500 MPa, and total true strain of 95%.

3.2. Creep response

Tensile creep tests were conducted in the temperature range of 973–1033 K with the applied stresses from 55 to 110 MPa. Fig. 3(a)

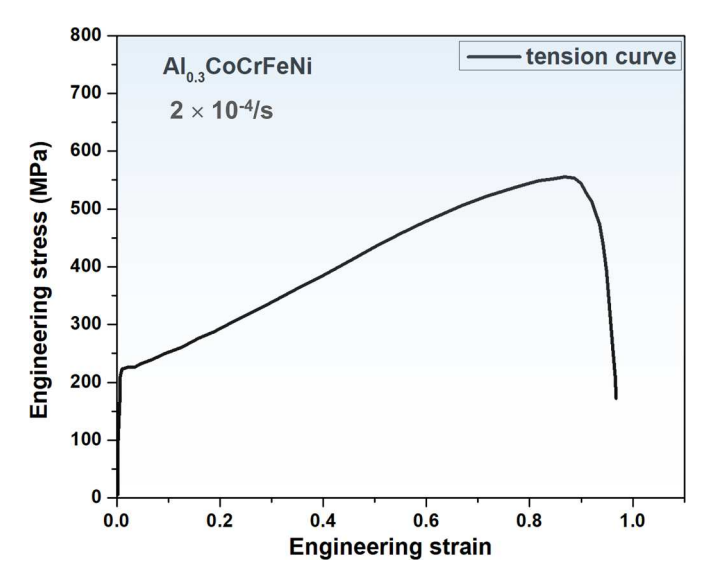


Fig. 2. The tensile engineering stress versus strain at room temperature.

displays the example creep curves (strain vs. time) of the $Al_{0.3}$ CoCrFeNi alloy at 973, 1003, and 1033 K under applied stress of 65, 75, 85, and 110 MPa. Generally, creep curves exhibit three typical stages. Upon initial loading, strain occurs at a relatively rapid strain rate, namely the primary stage. However, the rate gradually decreases with time until an approximately constant secondary rate is achieved. This is called the minimum creep rate, since it is the slowest creep rate during continuous loading. Eventually, the third stage (tertiary creep) displays much steeper creep-rate behavior. The strain rate continues to increase until

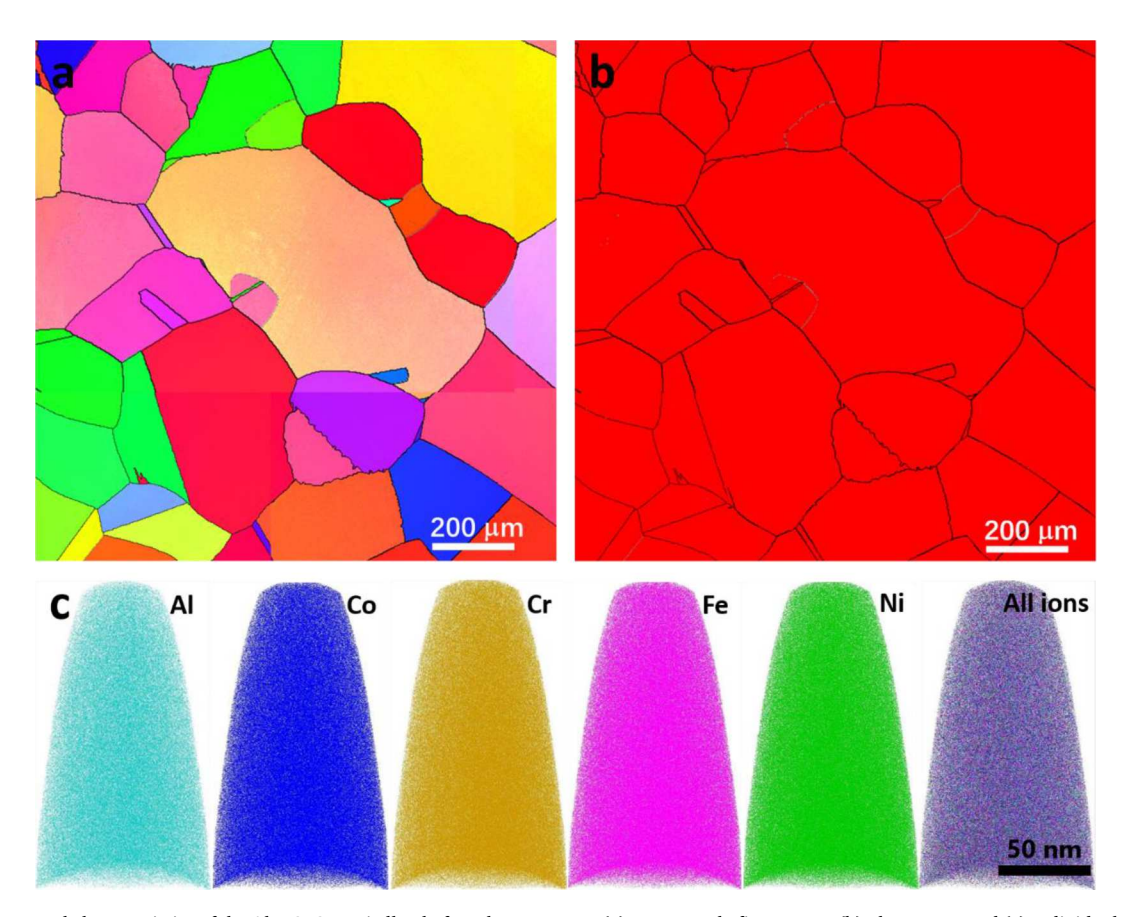


Fig. 1. Microstructural characteristics of the $Al_{0.3}$ CoCrFeNi alloy before the creep test. (a) Inverse pole figure map. (b) Phase map, and (c) Individual elemental maps, including Al, Co, Cr, Fe, and Ni, respectively.

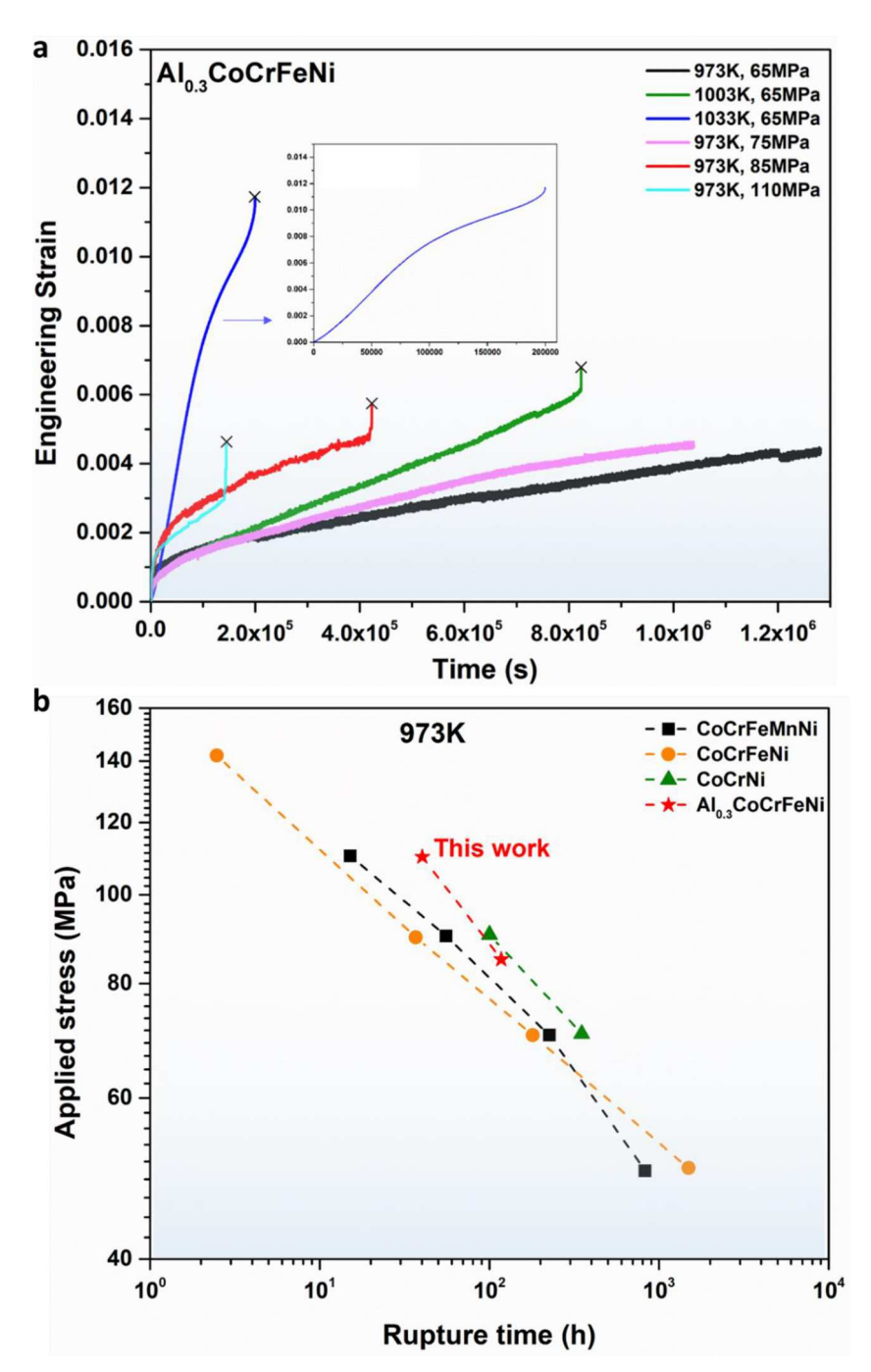


Fig. 3. (a) Example creep curves of $Al_{0.3}$ CoCrFeNi alloys crept in the temperature range of 973–1033 K under applied stress of 65, 75, 85, and 110 MPa. (b) The comparison of applied stress vs. rupture time in CoCrFeNnNi, CoCrFeNi, CoCrNi, and $Al_{0.3}$ CoCrFeNi alloys. Results of the Cantor subset alloys are taken from our previous work [33].

failure occurs, as indicated by the cross symbol in Fig. 3(a), due to the grain boundary cavitation and/or other damage processes. The curve shape and minimum creep rate are significantly affected by the testing temperature. At 1033 K, no primary stage is observed, and the specimen directly enters the secondary stage. Evidently, the specimen that crept at 1033 K/65 MPa has a larger minimum creep strain rate and shorter creep rupture life than that at 973 K/85 MPa. Since the primary creep is controlled by the competition between the work hardening and recovery [19], it depends strongly on the initial dislocation substructure and density. In some conditions, the third stages take less time, due to the damage progression on the grain boundary. Moreover, the rupture times depending on various applied stresses were displayed in Fig. 3(b) for

CoCrFeMnNi, CoCrFeNi, CoCrNi, and $Al_{0.3}$ CoCrFeNi alloys. It is apparent that the creep lifetime of $Al_{0.3}$ CoCrFeNi is higher than that of CoCrFeMnNi and CoCrFeNi alloys at the same applied stress. Additionally, the data points of $Al_{0.3}$ CoCrFeNi are close to those of the CoCrNi alloy, which follows the same linear relationship and indicates that $Al_{0.3}$ CoCrFeNi has a comparable or slightly longer creep life than the reported HEAs and ferritic steels [18].

3.3. Microstructural evolution during creep

To study the microstructural evolution during creep, the creep tests at 973~K and 75~MPa were interrupted at 50~h, 150~h, and 250~h,

respectively. In Fig. 4, red and white arrows represented the NiAl-rich and Cr-rich phases, respectively. The crystal structure of both phases would be confirmed in the following section. The yellow rectangle displayed the precipitate-free zone (PFZ). From the SEM image of the specimen that crept for 50 h, the irregular precipitates at the grain boundary are observed in Fig. 4(a). Most of these precipitates were confirmed as NiAl-rich phase, while the Cr-rich phase was occasionally observed as well by the SEM-EDS mapping, which was presented in Supplementary. A few needle-like and granular precipitates within the grain interior were formed and identified as NiAl-rich phase. With the creep time prolonging to 150 h, similar irregular precipitates are displayed at the grain boundary, with increasing density of granular and needle-like precipitates within grain interior, as shown in Fig. 4(b). When the creep test extended to 250 h, more lath- or needle-like precipitates with various orientations within grain interior were formed. Also, the density of small granular precipitates slightly declined as shown in Fig. 4(c), which is similar to the previous investigation [32]. Due to the limited size of the precipitates and the accuracy of the SEM energy dispersive X-ray spectroscopy (EDS), the compositions and crystal structures of the existing precipitates will be measured and characterized in the following section.

The three-dimensional (3D) APT reconstruction is performed to study the elemental distribution of the constituent atoms and segregation during the creep tests. The atom maps of the FIB-lifted-out samples taken from the region within a maximum of 1 μ m from the grain boundary are indicated in Fig. 5. Fig. 5(a) shows the ion maps of various elements resulting from the specimen that crept for 50 h. An interface between two phases, the Cr-rich phase, and the matrix, is captured in the dataset. A 30% at% Cr isoconcentration surface was used to delineate the interface between the matrix and Cr-rich precipitates with the proximity histogram shown in Fig. 5(a). The Cr-concentration curve increases from 24 to 55 at% from the matrix to nano-precipitates interiors, whereas the other elements (Al, Co, Fe, and Ni) decrease. This is especially true for the Ni concentration, which indicates that the nanoparticle was dominantly composed of Cr with minor Fe and Co elements again in consistence with previous reports [32].

The presence of the Cr-rich phase was observed in previous studies, such as CoCrFeMnNi [21,33], $Al_{0.3}$ CoCrFeNi [34], and Al_x CoCrFeMnNi [35]. Lee et al. [36] observed that the Cr-rich precipitates formed at dislocations within the grain interior or developed heterogeneously at grain boundaries during the creep tests at different temperatures. The formation of the Cr-phase at the grain boundaries was due to the large grain boundary serving as easy diffusion pathways and preferential nucleation sites [37].

Fig. 5(b) displays APT atom maps and proximity histograms for the $Al_{0.3}CoCrFeNi$ alloy after 100 h of creep testing at 973 K and 75 MPa. The depletion or enrichment of each element in some regions reveals the granular precipitate in the elemental maps and its accompanied

compositional separation, as shown in the proximity histogram elemental concentration. The concentration variations of all elements were sharp at the phase boundary. On the precipitate side, Ni and Al concentrations almost reach 60 at% and 25 at%, respectively, whilst Co, Fe, and Cr are largely depleted. Also, the concentration of Ni in the precipitate is about three times that of Al, indicating Ni₃Al compounds with an L1₂ crystal structure [14]. The typical L1₂ precipitates are in the range of 14–70 nm. Furthermore, after the precipitation of the L1₂ phase, the FCC solid-solution matrix still retains a high-entropy character with four principal elements, as indicated by the proximity histogram. Hence, it is anticipated that the high-entropy character of the matrix will maintain its advantageous performance, such as sluggish diffusion and impeded dislocation movement, etc., combined with the extra hardening role of the ordered second phase [14].

The APT atom maps and proximity histogram for the $Al_{0.3}$ CoCrFeNi alloy after the 150 h creep test are exhibited in Fig. 5(c). Visible granular particles with sizes of $20{\sim}80$ nm and enriched with Al and Ni are embedded in the matrix. The proximity histogram presents that the Ni concentration of a particle is around 60 at%, comparable to that of 100 h tests, while the Al concentration increases to 35 at%, indicating that the constituent concentration of precipitates changes with prolonged creep time. Fe, Co, and Cr elements have similar concentrations of approximately 25 at% in the matrix with a slightly lower Ni content.

In Fig. 5(d), the APT atom maps and proximity histogram for the $Al_{0.3}$ CoCrFeNi alloy crept for 250 h are displayed. The proximity histogram reveals that one phase is enriched in Ni and Al, and the other one is marginally enriched in Fe, Co, and Cr. The size of a lath-shaped phase measured from the SEM image is over 150 nm, much larger than that of specimens that crept for a shorter time, consistent with the SEM results of Fig. 4. The proximity histogram shows that the Ni concentration decreases to 40 at%, whilst the Al content increases to 38 at%, compared with that of 150 h tests, indicating the formation of the NiAl phase with a B2-crystal structure.

Due to the restricted size of the APT tip, many other precipitates in the specimen maybe not included. A series of TEM characterization was conducted on the specimen deformed under different loads, temperatures, and durations to further reveal the microstructure evolution during the long-term testing and understand the deformation mechanism, as displayed in Figs. 6–10. Fig. 6 shows the deformed substructure near the grain boundary of the specimen with an applied stress of 75 MPa at 973 K interrupted for 50 h. Grain boundaries are decorated by two types of precipitates. The first occasionally observed precipitates with dark contrast are enriched in Cr and depleted in other alloying elements relative to the matrix (TEM electron dispersive spectroscopy (TEM-EDS) results are shown in Table S1 in Supplementary). The selected-area electron diffraction pattern (SAED) from zone axis = [110] and [112] in Fig. 6(b and c) reveal that the crystal structure of the Crrich precipitates has a lattice parameter of three times than the FCC

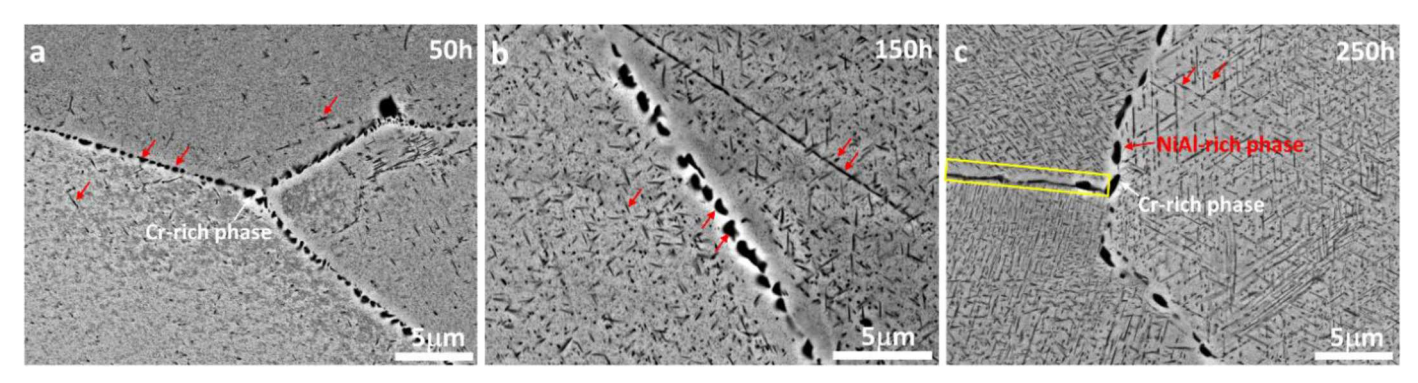


Fig. 4. SEM images of specimen tested at 973 K and 75 MPa interrupted for various durations: (a) Interrupted for 50 h. (b) 150 h, and (c) 250 h. Red and white arrows represent the NiAl-rich phase and Cr-rich phase, respectively. The yellow rectangle displayed the precipitate-free zone. (For interpretation of the references to colour in this figure legend, the reader is referred to the web version of this article.)

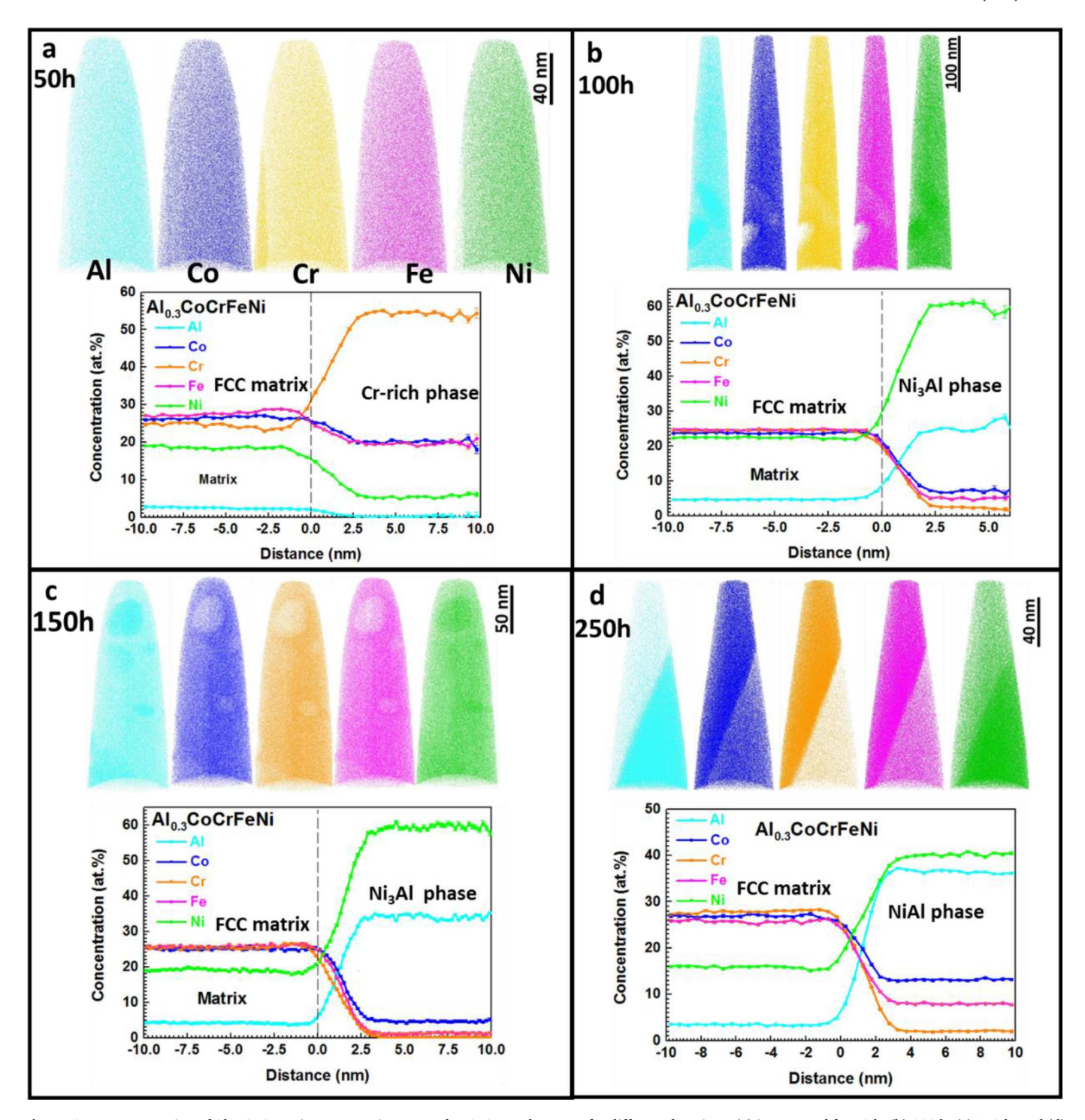


Fig. 5. APT reconstruction of Al_{0.3}CoCrFeNi creep tests interrupted at 973 K and 75 MPa for different durations: (a) interrupted for 50 h. (b) 100 h. (c) 150 h, and (d) 250 h.

matrix, consistent with $M_{23}C_6$. The formation of a carbon-containing phase is attributed to carbon contamination from either the melting furnace or the starting materials. The presence of $M_{23}C_6$ was also observed in the previous studies of the HEA specimens [38]. The TEM-EDS results presented in Table S1 imply that the total concentration of C in the matrix is very low and about 0.1%. The other frequently observed grain-boundary precipitates have a much higher volume fraction compared with that of $M_{23}C_6$. They are significantly enriched in Ni and Al, and also contain some Co and Fe but very little Cr, as given in Fig. S1 (Supplementary). The crystal structure was found to be ordered

B2 intermetallic phase according to the SAED result in Fig. 6(d). The high-resolution TEM (HR-TEM) from the interface between the B2 precipitate and matrix is outlined in Fig. 6(e). The corresponding FFT images show the perfect superposition of the $[110]_{FCC}$ ZA SAED from the matrix with the superposition of the $[111]_{BCC}$ ZA SAED from the precipitate in Fig. 6(f), which display the Kurdjumov-Sachs (K-S) type of orientation relation (OR) between the B2 precipitate and the FCC matrix. The appearance and chemical composition of these precipitates are also consistent with the grain-boundary phase observed recently by Gwalani et al. [39].

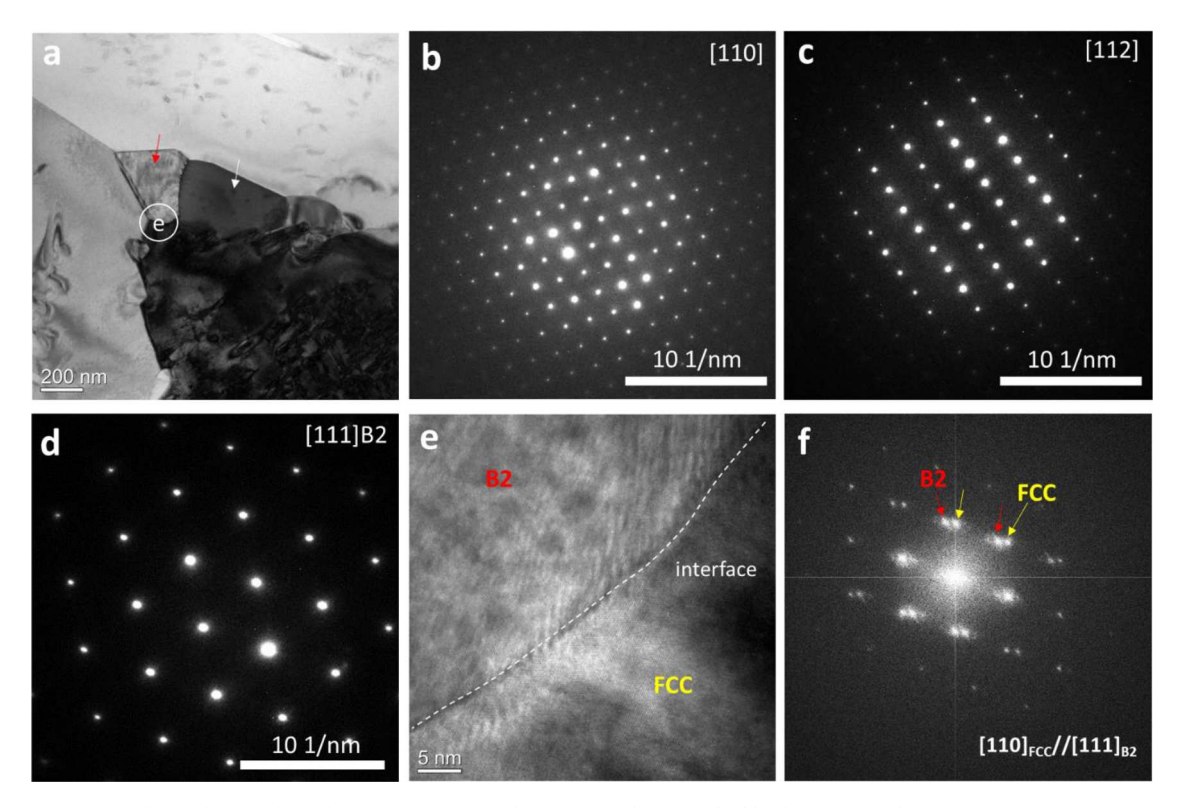


Fig. 6. (a) Precipitates at and near the grain boundary after creep for 50 h at 973 K under an applied load of 75 MPa. (b, c) SAED patterns of precipitate indicated by the white arrow in (a) recorded from [110] and [112] $M_{23}C_6$ zone axis, respectively; (d) SAED pattern of B2 precipitate indicated by the red arrow in (a) recorded from [111] B2 zone axis; (e) HR-TEM micrograph of interface between FCC and B2 precipitate (region marked as a white circle); (f) FFT image corresponding to FCC-B2 interface in (e). The red and yellow arrows in (f) represented the diffraction pattern of the B2 and FCC matrix, respectively. (For interpretation of the references to colour in this figure legend, the reader is referred to the web version of this article.)

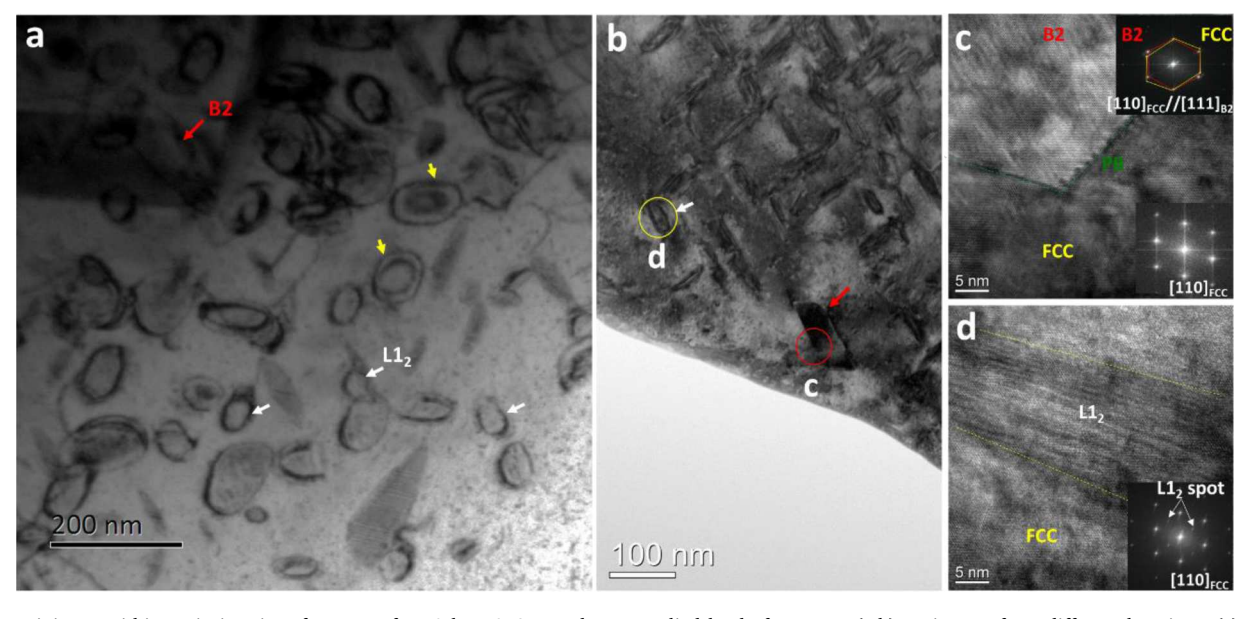


Fig. 7. Precipitates within grain interior after creep for 50 h at 973 K under an applied load of 75 MPa. (a,b) BF images from different locations. (c) HR-TEM micrograph of the interface between FCC and B2 phase, indicated by the red circle in (b). (d) HR-TEM micrograph of the $L1_2$ phase, indicated by a yellow circle in (b). The red, white, and yellow arrows in (a) represented the B2, $L1_2$, and dislocation loops, respectively. (For interpretation of the references to colour in this figure legend, the reader is referred to the web version of this article.)

Fig. 7 presents the deformed substructure within the grain interior in the specimen that crept at 973 K with an applied stress of 75 MPa for 50 h. The bright field TEM (BF-TEM) images from different locations show round and lath-like precipitates in Fig. 7(a) and (b). The HR-TEM images from marked regions of c and d in Fig. 7(b) are illustrated in Fig. 7(c) and

(d). A clear phase boundary between the precipitate and FCC matrix is observed in the HR-TEM image (Fig. 7(c)). The FFT of phase boundary between the lath-like precipitate and matrix in the inset of Fig. 7(c) confirms the $[111]_{B2}$ parallel to $[110]_{FCC}$ matrix. It is suggested that the B2 phase is primarily located at FCC grain boundaries. The production of

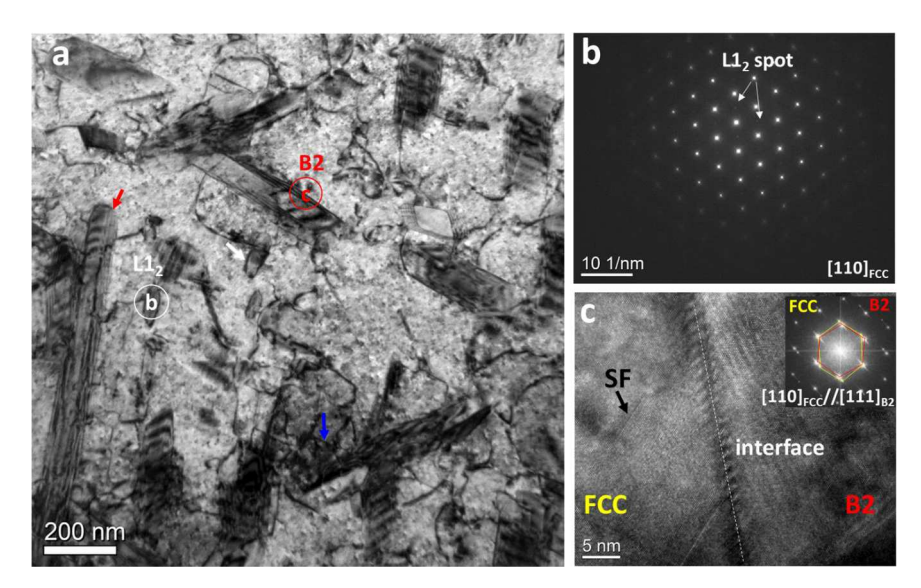


Fig. 8. (a) TEM micrographs of specimen crept at 973 K under 75 MPa for 250 h. (b) Diffraction pattern from FCC matrix and L1₂ recorded from [110] FCC zone axis (marked with b in (a)). (c) HR-TEM of the FCC-B2 interface. The red, white, and blue color in (a) represented the B2, dislocation loops, and dislocation tangles, respectively. (For interpretation of the references to colour in this figure legend, the reader is referred to the web version of this article.)

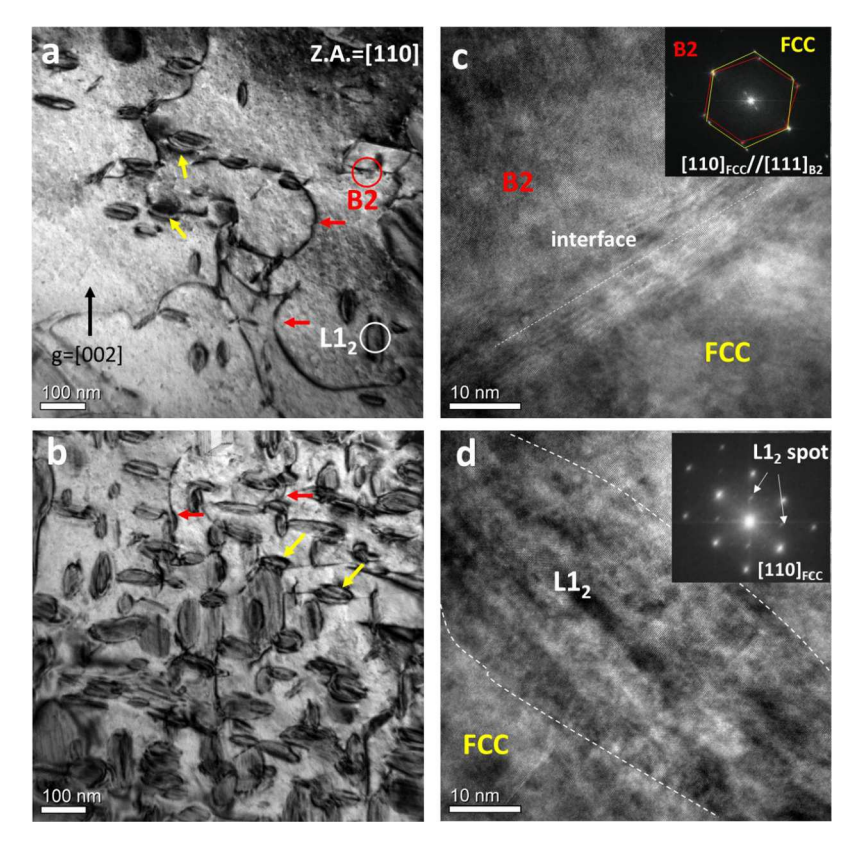


Fig. 9. TEM characterization of specimen deformed at 973 K under the applied load of 110 MPa (a), (b) BF images from different locations. (c) HR-TEM image of the phase boundary between B2 and FCC. (d) HR-TEM image of the FCC and $\rm L1_2$ precipitate. The corresponding FFT images of B2 and $\rm L1_2$ phase were shown in the inset. The red and yellow colors represented the bowed dislocations and dislocation loops. (For interpretation of the references to colour in this figure legend, the reader is referred to the web version of this article.)

a high-density ordered B2 phase is frequently reported owing to the strong negative enthalpy in the Al-Ni system [32]. Fig. 7(d) shows the FFT of $[011]_{FCC}$ zone axis(ZA) with extra superlattice spots at $\{100\}$ and $\{110\}$ locations, indicating the L1 $_2$ crystal structure. Previous studies showed that the L1 $_2$ precipitates were stable in the temperature range of 823–973 K in the Al $_0$ 3CoCrFeNi alloy [40,41]. The formation of the L1 $_2$ phase in Al $_2$ CoCrFeNi HEAs was determined by the ex situ as well as *in situ* TEM experiments at 973 K [39,42]. The lowest mixing enthalpy of Ni-Al among all the atomic pairs in the Al $_0$ 3CoCrFeNi HEA provides a thermodynamic driving force for the generations of phases rich in Ni and

Al elements. Less elemental diffusion is needed for the formation of the L1 $_2$ phase since the nucleation of the L1 $_2$ phase began with a short-range chemical rearrangement [43]. The volume fraction of L1 $_2$ is much higher than that of the B2 phase within the grain interior. Dislocation loops (indicated by the yellow arrow) and bowed dislocations are found in the matrix. Due to the limited creep strain of 0.001 for creeping samples that were interrupted for 50 h, the density of dislocation and dislocation loops was very low.

As the types and composition of precipitates generated at the grain boundaries from different loading conditions are quite similar, only TEM

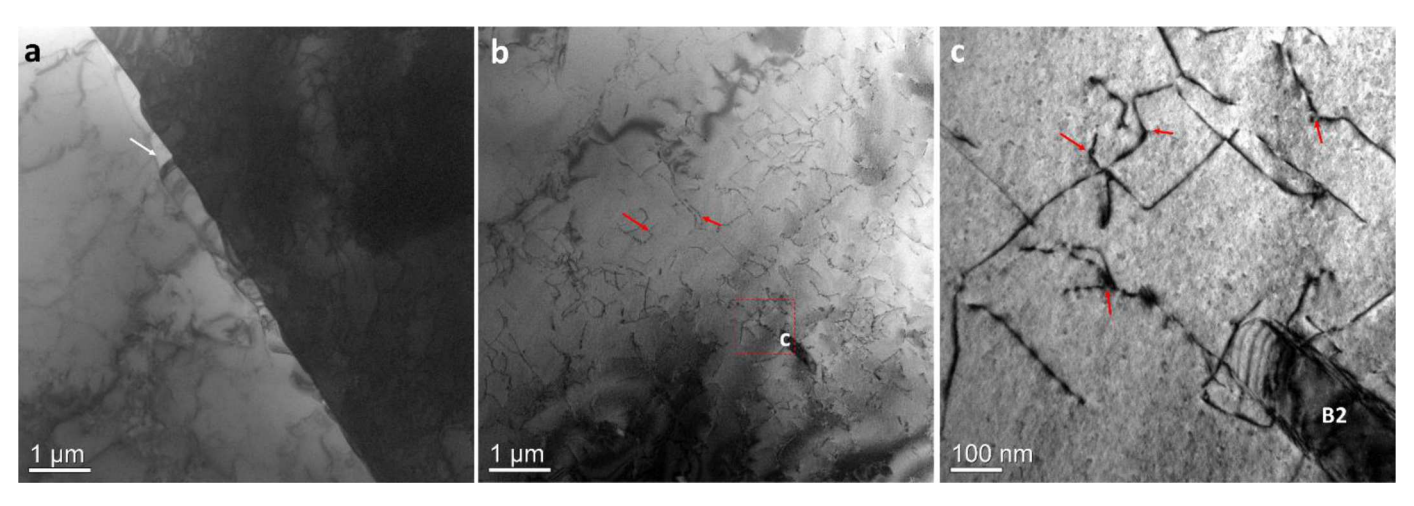


Fig. 10. TEM of specimen deformed at 1033 K under 75 MPa. (a) Boundary-precipitates (indicated by white arrow) and high density of dislocation within the grain interior. (b) High density of bowed dislocations within grain interior. (c) A higher magnification image (marked with c in (b)) exhibiting apparent dislocation-lattice and dislocation-dislocation interactions. The B2 phase was occasionally observed. The red arrows represented the pinned dislocations by the high entropy matrix. (For interpretation of the references to colour in this figure legend, the reader is referred to the web version of this article.)

results of grain interior will be given in the following specimens. Fig. 8 (a) shows the BF-TEM image of precipitates and dislocations in the specimen deformed at 973 K under 75 MPa and interrupted for 250 h. There was an increase in the density of dislocations when compared to the 50 h specimen. In addition to dislocation loops dislocation pileups, multiple dislocation tangles as well as stacking fault fringes were frequently observed, as shown in Fig. 8(a) and (c). The SF fringes are the typical characteristic of the dissociation of perfect dislocations. The dissociation of perfect dislocations into partial dislocations generates stacking faults (SFs), which prevent the glide of other dislocations passing through the SF planes, which will result in an increase in the strength of alloys. A high number of dislocations aggregate and entangle with each other around the lath-like phase, as shown in Fig. 8(a), resulting in an inhomogeneous distribution that indicates a dislocationmediated deformation mechanism. The SAED patterns of the FCC matrix and round precipitates are presented in Fig. 8(b). The existence of a superlattice indicates the L1₂ intermetallic phase that pinned the mobile dislocations to form the loops, as indicated by the white arrow. The HR-TEM of the interface between B2 and FCC is presented in Fig. 8(c), with the FFT in the inset. Similarly, the B2 precipitates present the K-S OR with the FCC matrix, as revealed by the FFT image. The compositions of the present B2 phase are revealed as \sim 40 at% Ni and \sim 38 at% Al by the APT analysis, which suggests that Ni and Al atoms alternatively occupied the lattice position in the B2 unit cell, while other component atoms are substitutional solution atoms [44]. These lath-like B2 particles act as obstacles to pin the mobile dislocation and form the dislocation tangles, as indicated by the blue arrow. Additionally, the volume fraction of lath-like B2 precipitates is much higher than that of the L12 phase.

To compare the deformation mechanism under different applied loads, the microstructure of the specimen crept at 973 K and 110 MPa is presented in Fig. 9. Fig. 9(a) and (b) exhibit the precipitates and dislocations obtained from different locations in one sample. The HR-TEM images from these two different precipitates are exhibited in Fig. 9(c) and (d). Similarly, the corresponding FFT images presented in the inset reveal the presence of the B2 and L1 $_2$ phases. These B2 particles have a definite orientation relation with the parent FCC matrix. No other new phase is found after the creep at 973 K and 110 MPa. It should be noted that the L1 $_2$ precipitates are mostly observed with minor B2 precipitates, as demonstrated in Fig. 9(a) and (b). Apparently, many L1 $_2$ precipitates interact with mobile dislocations and form dislocation loops or bowed by particles as indicated by yellow and red arrows in Fig. 9(a) and (b).

Fig. 10 presents the deformed microstructure of the specimen crept at 1033 K and 75 MPa for 20 h. No apparent precipitates within the grain

interior are found; instead, many grain-boundaries precipitates appeared, as displayed in Fig. 10(a), which may be due to the short time of the creep experiment. In order to reveal the effect of creep time and temperature on the precipitate generation, an annealing treatment of $1033~\rm K$ on an as-homogenized sample was carried out for $20~\rm and~50~h$. Many precipitates were found at the grain boundaries and within the grain interior for $50~\rm h$ instead of $20~\rm h$ (shown in Fig. $20~\rm h$), explaining the absence of precipitate within grain the interior after creeping at $1033~\rm K$ for $20~\rm h$. In Fig. $20(a)~\rm and$ (b), a high density of dislocations was obtained after creep. The extensive sharply curved dislocations (indicated by red arrows) were frequently found in the magnified Fig. $20~\rm c$, which implied the strong interaction between the forest dislocations. The competition between $20~\rm c$ and $20~\rm c$ precipitation evolution would be explained in Fig. $20~\rm c$ to better understand the distinctive consequences of these two types of precipitates on the creep performance.

3.4. Fracture morphologies of crept samples

Fractography provides an efficient way to study the fracture mechanism of the Al_{0.3}CoCrFeNi alloy. Similar to conventional alloys, the fracture surfaces of HEAs can be categorized as ductile or brittle fractures. After creep tests at 973 K and stress levels of 55, 75, and 110 MPa, fracture surfaces of the crept samples were investigated using scanning electron microscopy (SEM) in order to understand the mechanical properties, as shown in Fig. 11. The overview of the fracture surfaces for three specimens is displayed in Fig. 11(a)-(c). Higher magnifications of these surfaces are presented in Fig. 11(d)-(f). It should be noted that many small particles were confirmed to be oxides distributed in the fracture surface when the specimen is subjected to long-term exposure at 973 K. Moreover, typical ductile fractures with a high density of dimplelike structures can be observed on the fracture surfaces at all three stress levels. A dimple-like structure is related to microvoid coalescence or aggregation [45], which is a typical feature of ductile fracture caused by the synergistic interactions of dislocations and microvoids.

4. Discussion

4.1. Microstructure evolution

According to the thermodynamic calculation [15,27,41], the $Al_{0.3}$ CoCrFeNi FCC solid solution is metastable at 973 K. Consequently, there is a thermodynamic possibility for the production of new phases. Three thermodynamic stable phases are the FCC, B2, and σ phases,

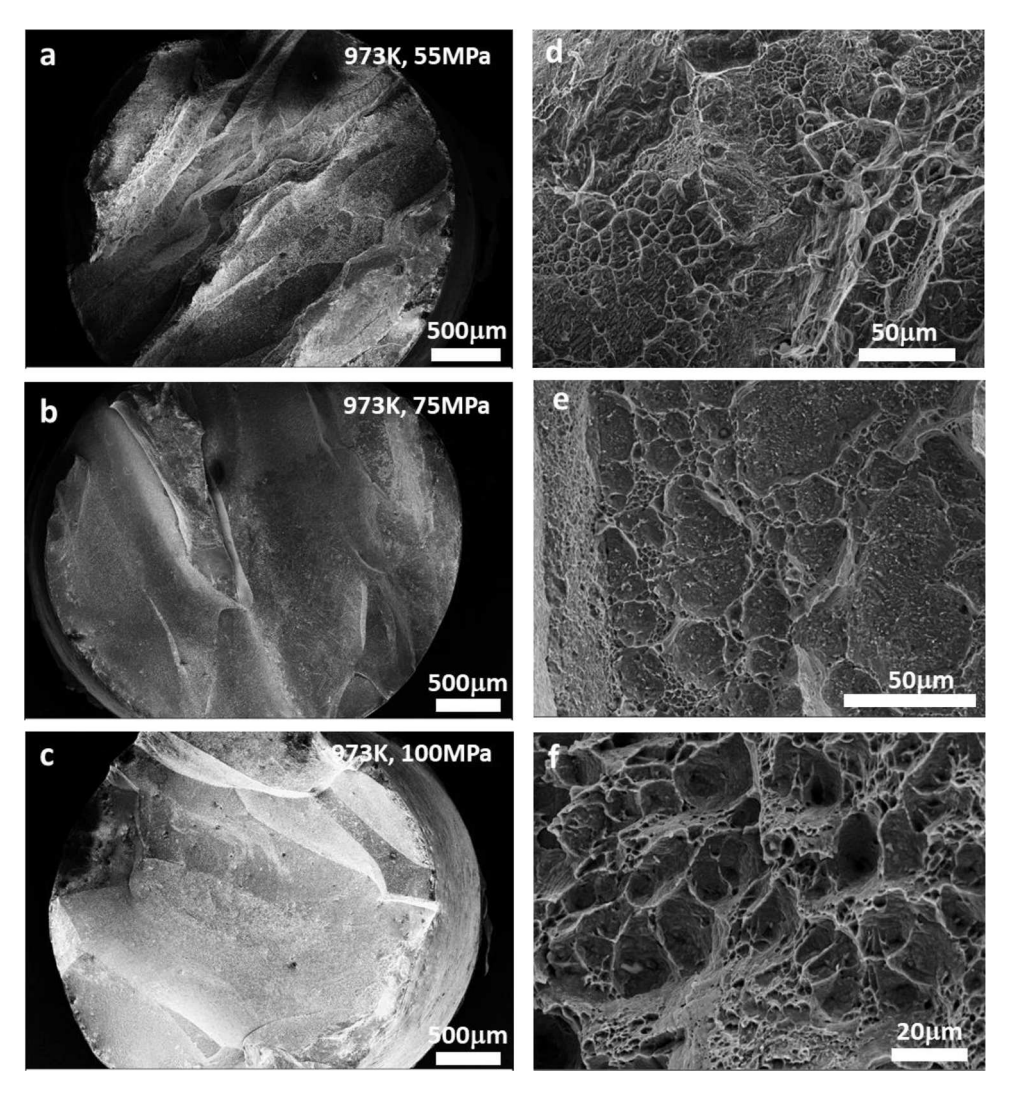


Fig. 11. Fracture morphologies of the crept specimens at 973 K under various applied stresses. (a)(d) 55 MPa, (b)(e) 75 MPa, (c)(f) 100 MPa.

whilst the present study did not capture the presence of the σ phase in the TEM images due to their low density and the restricted area. However, a new phase of an L1₂ compound was found during the long-time creep as displayed in APT and TEM. That is, despite the fact that the ordered L12 phase is not thermodynamically stable at this temperature, as determined by the equilibrium phase fractions based on the thermodynamic model predictions [32], it has been regularly detected in the annealed alloys [46-48]. Similarly, Gwalani et al. [39] found both L12 and B2 phases in the fully recrystallized specimen annealed at 893 K, disagreeing with the model prediction. However, when the cold-rolled sample was directly subject to the annealing without recrystallization, B2 forms without any L12, indicating that thermo-mechanical processing may affect the solid-solid phase-transformation pathway. There is competition between different precipitate types based on the description of Gibbs free energy curves, which can be explained in terms of kinetics of precipitate nucleation.

At 973 K, the B2 phase possesses the highest driving force of the three phases, while σ and L1 $_2$ phases have similar driving forces, with L1 $_2$ being slightly larger. From the thermodynamic point of view, the phase diagram prefers the occurrence of the B2 phase, and long-term annealing experiments have validated this tendency [32]. The lattice constant of the B2 phase was estimated to be 0.2882 nm. Even in the form of the KS OR, there will be a large lattice mismatch, comprised of both contraction and shear components. The shear mismatch is responsible for the lath shape. The contraction, on the other hand, leads to a novel phenomenon

here. In the classic work by Eshelby, an inclusion with a phase-transformation strain of ε_{ij}^T interacts with a faraway applied stress field $\sigma_{ii}^{applied}$, leading to the excess free energy of

$$\Delta G = -\int\limits_{inclusion} \sigma_{ij}^{applied} \varepsilon_{ij}^T dV \tag{1}$$

where the integral is carried over the inclusion or second phase. A summation convention is assumed for repeated indices. The inner product of uniaxial tension and a contraction component in the KS OR will lead a positive energy, thus leading to an energy penalty term. In other words, the driving force for the B2 phase nucleation is reduced. This is the thermodynamic reasoning for B2 precipitation process being suppressed Eqs. (1) and (2).

From the kinetic point of view, based on the available values for Ni-and Co-based superalloys, the predicted interfacial energy of FCC/L1 $_2$ is very low of ~ 10 –40 mJ/m² [48], leading to a low nucleation barrier for the L1 $_2$ phase. On the other hand, the B2 and σ phases both exhibit a semi-coherent or incoherent interface with the FCC matrix, respectively. The interfacial energies of the FCC/B2 and FCC/ σ were estimated as 180 mJ/m² in Fe-Ni systems and 500–800 mJ/m² in steels [40], respectively. These values are significantly larger than the predicated interfacial energy and may result in a higher value of the nucleation barrier. At the early stage of creep tests, the HEA specimen is almost strain-free. Thus, few defects exist in the matrix, similar to that of the fully-recrystallized

state [39]. Although L1₂ is a metastable phase from a thermodynamic viewpoint, a lower nucleation barrier for the L12 phase may have a substantial onset driving force at 973 K in the FCC solid solution, resulting in L12 precipitation. In contrast, grain boundaries are the preferential heterogeneous nucleation sites and the lower value of the nucleation barrier for the B2 phase. Hence, the B2 phase formed at the matrix grain boundaries as shown in Fig. 10. The generation of the L12 phase may be promoted due to a higher homogeneous nucleation rate than other competing equilibrium phases. As the creep proceeded and time increased, increasingly lath-like B2 precipitates formed within the grain interior attributed to the favored thermodynamic promotion. While the nucleation and growth of the L12 phase will be restricted or reduced due to the competition of the constituent of Ni and Al, the number of L12 is still very high in specimens interrupted at 150 and 250 h. The applied load effect of 75 and 110 MPa on the precipitation is very limited (Figs. 7 and 9), indicating that the thermodynamic and kinetic effect is the dominant factor for L12 and B2 formation. The APT and the SEM results of the specimen interrupted for various times displayed the formation of the Cr-rich phase as well as the Ni-Al-rich phase, which was also observed in the previous study [49], since the formation of these features is governed by a complex diffusion mechanism. With the prolonged creep time, the Ni-Al-phase formation now dominates the precipitation behavior because of their larger driving force, as discussed above. L12 phase formation will be gradually inhibited by the B2 phase due to the enhanced instability, leading to an increase of the nucleation rate of B2 phase. The B2 phase formed during creep tests has a similar chemical concentration but with a lower concentration of Al than the preliminary B2 phase. From the chemical perspective, the formation of the B2 phase would induce a Ni and Al deficit in the surrounding region and a subsequent increase in the concentration of Co, Fe, and Cr. This would provide favorable conditions for the creation of the Cr-rich phase. Moreover, the Cr-rich phase appears to nucleate and develop heterogeneously at grain boundaries and triple junctions, or adjacent to the B2 phase, whilst maintaining an orientation relationship with the B2 precipitate [47].

In the TEM images of the interrupted sample at 973 K under 75 MPa in Fig. 8, visible stacking faults are widely observed, suggesting the movement of numerous Shockley partial dislocations [15,16]. It is assumed that the motion of Shockley partial dislocations accommodates the strain in the deformation process and reduces the dislocation storage, resulting in a strain release. No nucleation of twins was triggered at 973 K. Evident dislocation segments, dislocation-dislocation, and dislocation-precipitate interactions were observed in the TEM images, resulting in the formation of intensive dislocation tangles, accumulation around particles, and bypassing loops. These features could be barriers to the dislocation movement. No dislocation climb was found due to the insufficient temperature that is not capable of activating the thermal climbing process to overcome the precipitate barrier. As the applied load increases to 110 MPa at 973 K, the dislocation loops were mostly observed in the matrix, which was attributed to the strong interaction of L12 precipitates and mobile dislocations. No apparent shearing particle by dislocations was observed. When the creep temperature increased to 1033 K, no precipitates were produced because of the short creep time, and deformation is mainly controlled by the dislocation glide. The sharply curved dislocations indicated by red arrows in Fig. 10(b) and (c) may be caused by the strong interaction between forest dislocations.

Generally, there are two main deformation mechanisms, either through a dislocation bypass (Orowan-type) or particle shearing mechanism, for precipitation hardening. In the present work, no dislocation sheared precipitates, but multiple bypassed loops and bow-out dislocations were found in the matrix, indicating the movement mechanism of dislocations should be mainly the Orowan bypassing. These precipitates generated during the creep experiments, in general, present complicated obstacles to dislocation migration and accelerate sluggish diffusion kinetics. Coupled with the low stacking fault energy, the Al_{0.3}CoCrFeNi alloy is expected to possess exceptional strengthening at elevated

temperatures and balanced creep resistance. A more quantitative assessment of Orowan stress will be provided shortly.

4.2. Creep resistance/mechanisms

Conventional creep tests are mainly concerned with the steady-state empirical scaling law between the creep rate and the stress, where the exponent parameter suggests the creep mechanism: diffusion-controlled or dislocation-movement-controlled [50]. Considering creep as a thermally activated phenomenon, creep behavior is usually characterized by the following equation [51]:

$$\dot{\varepsilon}_{min} = A\sigma^n \exp\left(-\frac{Q}{RT}\right),\tag{2}$$

where $\dot{\varepsilon}_{\rm min}$ is the minimum creep rate, A is a material-dependent constant, σ is the applied stress, n is the stress exponent, Q is the apparent activation energy, R is the gas constant, and T is the absolute temperature of creep tests.

Fig. 12 showed the dependence of the minimum creep rate on stress and reciprocal temperature. Fig. 12(a) displayed that the logarithm of the minimum creep rate exhibited a linear relationship with the logarithm of the stress. This trend suggested that the HEA specimens exhibited the power-law creep behavior. The stress exponent determined by the slope increased with the increase of the test temperature, which is consistent with other HEAs [20,27,34]. Typically, the value of the stress exponent is thought to represent the deformation mechanism during creep tests. The stress exponent of the specimens can be determined to be 3.0 - 6.53, which suggests that the deformation mechanism is mainly dominated by dislocation glide and dislocation climb [18] at low-stress exponent and precipitate hardening at high-stress exponent. Since no dislocation climb or precipitate shear events were observed in the TEM images, only dislocation gliding controls the deformation, as evidenced by the event of dislocations looping around precipitates in the alloy crept at 973 K with 75 and 110 MPa, accompanied by dislocation bowing. A general glide and bypass of the dislocation mechanism is likely to explain the present TEM observation and stress exponent. The stress exponent of 6.53 seen in the present work is significantly higher than single-phase Cantor alloys, due to the strong precipitate hardening of $Al_{0.3}$ CoCrFeNi with a high volume fraction of $L1_2$ and B2 phases.

Fig. 12(b) presents that the logarithm of the minimum creep rate also exhibits a linear relationship with the reciprocal temperature. The apparent activation energy of the creep deformation can be determined to be $390-548.2 \text{ kJ} \cdot \text{mol}^{-1}$ by the slope of 65-110 MPa. It is clear that the 390 kJ·mol⁻¹ at 65 MPa is consistent with the previous study of 393.58 kJ·mol⁻¹ [28] and slightly higher than the 370 kJ·mol⁻¹ of CoCrNi medium-entropy alloys [18], and 330 kJ·mol⁻¹ of CoCrFeMnNi alloys [52]. The higher activation energy of 470.2 and 548.2 at 75 and 110 MPa, respectively, may be attributed to the strong effect of interaction between precipitates and mobile dislocation. It is discovered that the high-stress exponent and activation energy in the nickel-based superalloy could be attributed to the γ' strengthening effect. The uniform dispersion distribution of large amounts of secondary precipitates in the FCC matrix causes a significant barrier to the dislocation movement, which would heavily influence the creep behavior. For example, the specimen held at 973 K and 75 MPa interrupted after 250 h has a total volume fraction of L12 and B2 phase approximately as high as 19%, explaining why a higher stress exponent, as well as activation energy, was obtained in Al_{0.3}CoCrFeNi.

For a better comparison and understanding of creep behavior, a compilation of the stress exponents and activation energies from other studied HEAs at various temperatures and applied stresses is plotted in Fig. 13, and detailed in Table 1 [4,18,20,21,24–28,34,51,53–58]. Apparently, the calculated activation energy vs. stress exponent of all the studied HEAs roughly displayed a linear dependence, as marked by the red oval in Fig. 13. Moreover, the most studied CoCrFeMnNi HEA

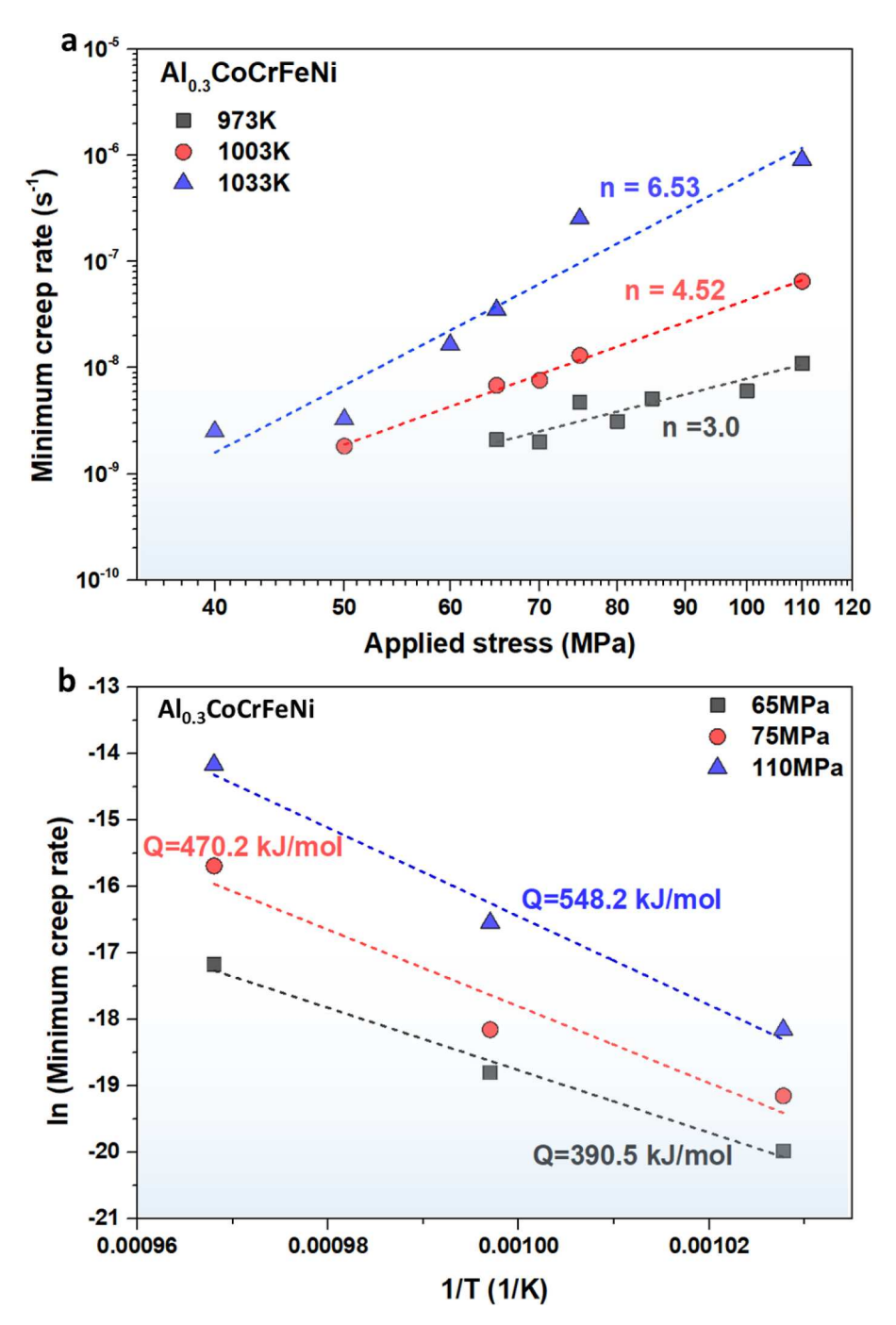


Fig. 12. (a) Double logarithmic plot of applied stress vs. steady-state strain rate. (b) Logarithm plot of steady-state creep rate vs. temperature reciprocal for the Al_{0.3}CoCrFeNi alloy.

indicated by black symbols displays a range of stress exponents of 3–6.3 and activation values of 230–330 kJ·mol⁻¹, suggesting that the creep properties largely depend on the thermomechanical processing routes and testing conditions. Only one n value in a study performed by Cao et al. [56] was as high as 8.9, which was ascribed to the coordinative contributions of distinct dynamic recrystallization and precipitation along grain boundaries, along with the dislocation tangling configurations. The result was the ability to significantly block the dislocation movement, leading to an abnormally high stress exponent and activation energy at higher stress levels. Kang et al. [24] found that with the stress exponent of 3.7 and activation energy of 230 kJ·mol⁻¹, the creep behavior in CrMnFeCoNi relies heavily on thermal activation with the majority of creep strengths coming from solid-solution hardening,

especially at low applied stresses. The rate-controlling deformation mechanisms in CoCrFeMnNi are dislocation-solute interactions and forest-dislocation interactions. The creep mechanism transforms from the climb-controlled creep to viscous glide creep by changing the applied stress, based on the calculation of the stress exponents and activation energies in another CoCrFeMnNi [22]. The abnormally high stress exponent of 10.8 from Al $_1$ Co $_2$ SCr $_8$ Fe $_1$ SNi $_3$ GTi $_6$ alloy was attributed to the remarkable interaction of mobile dislocations with a large amount of γ' precipitate in the matrix. Particularly, the highest stress exponent of 13.2 and the corresponding activation energy of 580 kJ·mol $^{-1}$ located at the very top right of the map was obtained from oxide-dispersion strengthened (ODS) CoCrFeMnNi HEA. Generally, ODS alloys always exhibited distinct characteristics, such as anomalously

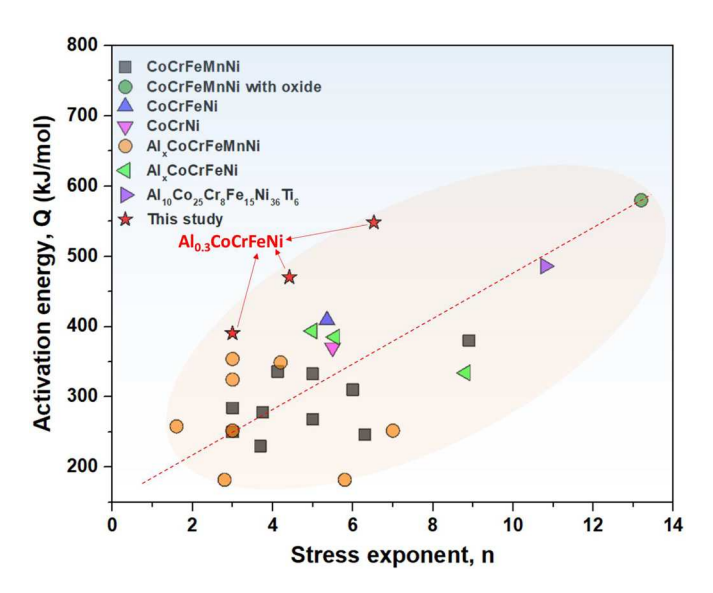


Fig. 13. The plot of the activation energy vs. stress exponent of various HEAs. See Table 1 for the data compilation.

Table 1Summary of stress exponents and activation energies in the present and previous HEAs.

Alloy	n	$Q/kJ \cdot mol^{-1}$	T/K	Stress/ MPa
CoCrFeMnNi [51]	3 at low	284	1023-1123	7–300
	σ _{app} 5 at high	333		
CoCrFeMnNi [20]	σ _{арр} 3.75	278	600–650	48–96
CoCrFeMnNi [21]	5.75 5–6 at low	268	773–873	140–400
COOR CHIRAL [21]	σ_{app} >8.9 at	~380	770 070	110 100
CoCrFeMnNi [24]	high σ_{app} ~6 at low	305–320	808-923	<40
	σ _{app} 3 at medium	235–250		>40
	σ_{app}			
CoCrFeMnNi [25]	6.3	246	973–1023	10–85
0.0 7.14.11	10.1	704	1023-1073	
CoCrFeMnNi with oxide	1.8 at low	210	973–1073	
[25]	σ _{app} 13.2 at	580		
C-C-E-M-N; FEO1	high σ _{app}	010.0	1000 1000	
CoCrFeMnNi [53] CoCrFeMnNi [23]	5 3.7	312.2 230	1023–1323 1023–1173	20-200
CrFeCoNi [27]	5.36–6.75	409	923–998	50 - 200
CoCrFeMnNi [27]	4.13–5.94	336	923–998	30 - 200
CoCrNi [18]	4.8–5.5	370	973–1073	
Al _{0.4} CoCrFeMnNi [34]	1.6–2.2 at	258	873–973	80-240
7110,4GOGIT CIVILITYI [34]	low σ _{app}	230	0/3-7/3	00-240
	4.2–4.9 at	349		
	high σ _{app}	0.15		
Al _{0.6} CoCrFeMnNi [34]	5.8	182-193	873	
0.0	2.8-3.5		923-973	
Al _{0.5} CoCrFeMnNi [26]	3–7	251.9	1023-1323	
AlCoCrFeMnNi [54]	3	353.8	1173-1373	
Al _{0.7} CoCrFeMnNi [55]	3	324.6	1173-1373	
Al _{0.3} CoCrFeNi [26]	> 5	393.58	1023-1223	
Al _{0.15} CoCrFeNi [56]	5.56	385	853-973	95-125
Al _{0.6} CoCrFeNi [56]	8.82	334		
CoNiCrAlY [57]	1-3.9	512-224	1073-1473	4-150
$Al_{10}Co_{25}Cr_8Fe_{15}Ni_{36}Ti_6$ [58]	10.8	486	973–1073	325–425
$Al_{0.3}$ CoCrFeNi This work	3-6.53	390.5-548.2	973–1033	40-110

Note: low/high $\sigma_{app}\!\!:$ creep test performed at low/high applied stress.

high-stress exponent and the existence of threshold stress. For example, this effect was also observed in previous nickel-based ODS alloys [59-61]. Such unique characteristics of ODS alloys were attributed to the interaction between dispersed particles and dislocations. Apparently, such an extremely high value in (ODS) CoCrFeMnNi HEA was caused by the strong oxide-dispersion strengthening effect in the Cantor alloy. No obvious transitions between different mechanisms are observed within the temperature and stress ranges tested in the present investigation. Since the reported activation energy in the solid-solution HEAs is in the range of 230–704 kJ·mol⁻¹, it is reasonable to obtain the 390-548.2 kJ·mol⁻¹ for the studied material in the present study. According to the fitted stress exponent and activation energy, combined with the TEM characterization, dislocation-precipitate interaction and dislocation-dislocation interaction are proposed to be the dominant creep deformation mechanism for this alloy in the temperature range of 973-1033 K.

4.3. Comparison of creep behaviors

The creep resistance (the secondary creep rate as a function of applied stress) and creep lifespan with the applied stress at 973 K were compared with CoCrNi [18], CoCrFeMnNi [23,24], Al_vCoCrFeMnNi [35], Al₁₀Co₂₅Cr₈Fe₁₅Ni₃₆Ti₆Hf [58], and several commercial ferritic steels [14] to acquire a clear image of the creep characteristics of the Al_{0.3}CoCrFeNi alloy. Fig. 14 shows that the Al_{0.3}CoCrFeNi alloy exhibited reduced minimum creep rates, e.g., $1 \sim 4$ orders of magnitude lower, as compared with other reported HEAs and commercial precipitate-strengthened ferritic alloys at the same stress level without much change in the rupture time. These results show that the present alloy should show a significant improvement in its elevated temperature properties. Such superior creep resistance in the Al_{0.3}CoCrFeNi alloy be attributed to the better combination of both solid-solution-strengthening and significant precipitate strengthening of L12 and B2 phases acting as the strong obstacles of the mobile dislocations than that of the previous alloys without particles (CoCrNi, CoCr-FeNi, and CoCrFeMnNi alloys), as displayed in the TEM analysis.

The high densities of $\rm L1_2$ and B2 particles, especially the coherent $\rm L1_2$ phase, are expected to produce significant precipitate hardening during the creep experiments, as supported by the APT and TEM observations. Generally, the mechanisms for precipitation strengthening can be divided into two categories, Orowan bowing or particle shearing, depending on the interaction between moving dislocations and

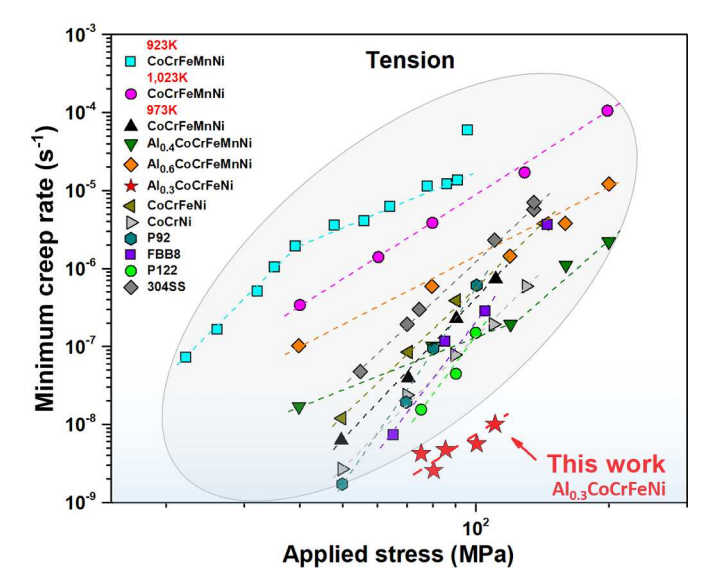


Fig. 14. Comparison of steady-state creep rate vs. applied stress curve in conventional alloys and HEAs.

precipitates. The Orowan mechanism generally occurs when the particles are large or incoherent with the matrix, while the shearing mechanism dominates when the precipitates are coherent and small [62,63]. It is estimated from the TEM results (Fig. 8) that the small L1 $_2$ nanoparticles with a lattice constant of 0.3541 nm are coherent with the FCC matrix with the lattice constant of 0.3598 nm, resulting in a small lattice misfit of 1.6%, but higher than the previous study of 0.2%. However, this may be due to the applied load during the creep experiment [64,65].

In the present work, even though the lattice misfit between $\rm L1_2$ precipitates and FCC matrix is as small as 1.6%, Orowan bypassing rather than shearing is mostly favored under both low and high applied load at 973 K (Figs. 7–9) due to the large size of $\rm L1_2$ and low applied stress. No dislocation shearing or loops are observed at 1033 K since the creep time is short for the formation of precipitates before failure.

The strength increment, $\Delta \sigma_{Orowan}$, is governed by the dislocation-bypassing mechanism and can be calculated with the equation [62,66]:

$$\Delta \sigma_{OR} = M * \frac{0.4Gb}{\pi \lambda_s (1 - v)^{\frac{1}{2}}} * \ln\left(\frac{1.63r}{b}\right),\tag{3}$$

$$\lambda_s = 0.82 * \left[\left(\frac{\pi}{f} \right)^{\frac{1}{2}} - 2 \right] * r, \tag{4}$$

where M = 3.06 (Taylor factor for an FCC structure); G = 88 GPa (shear modulus of the matrix), [31,64,67]; f = 14.4% (the volume fraction of the precipitates $L1_2$ from TEM results in Fig. S4(a)), r is in the range of 10–80 nm (the mean precipitate radius), $b = \sqrt{2} \times \frac{a_{fcc}}{2} = 0.254$ nm (the magnitude of the matrix Burgers vector) [32], λ_s is the inter-precipitate spacing, and v = 0.25 (Poisson's ratio) [68]. By applying the above equations, the calculated $\Delta\sigma_{OR}$ with varying radius was plotted in Fig. 15. It is usually observed in precipitation strengthening that, when the particle size is below a critical value, the shearing mechanism will control the deformation while bypassing will be dominant when the precipitate is larger than the critical value. However, the shearing process was not observed in our TEM characterizations. Generally, in the Orowan-bypassing mechanism, dislocations pass through the inter-particle region, and dislocation loops are created around precipitates, which is consistent with the TEM observation that many dislocation loops were generated in the matrix.

Considering the temperature dependence of the elastic constants, Laplanche et al. [69] showed that the shear modulus for CoCrFeNi alloy can be fitted to temperature by

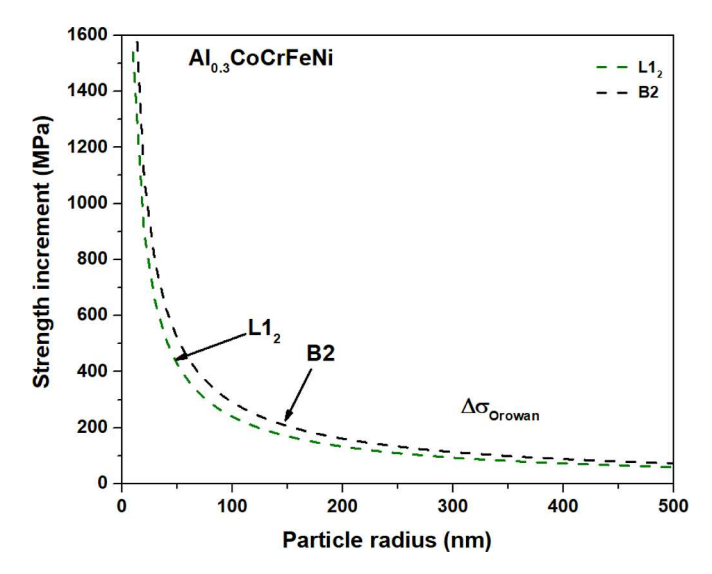


Fig. 15. The plot of $\Delta\sigma_{Orowan}$ of L1₂ in specimen deformed at 973 K and 75 MPa interrupted for 50 h and B2 interrupted for 250 h depending on the particle size, r.

$$G = G_{273K} - 13/(e^{373/T} - 1), (5)$$

where G_{273K} is the shear modulus at 273 K, the moduli are in the unit of GPa, and the temperature T is in the unit of Kelvin. While the change of shear modulus of our material with respect to temperature is not known, an estimate based on Eq. (5) gives a reduction from G=88 GPa to about 60.2 GPa. Subsequently, the Orowan bypass stress is found to be 230.0 MPa, using f=14.4% and r=80 nm, being reduced by 31.6% from 349.6 MPa when using the room-temperature shear modulus. It should be noted that the volume fraction f and the mean particle size r could not be estimated accurately based on limited TEM observations, and yet the Orowan stress in Eq. (5) is quite sensitive to these two parameters and the cutoff radius (taken as b/1.63). For example, a decrease of f from 0.14 to 0.10 (keeping f=80 nm) and an increase of f from 80 to 120 nm (keeping f=0.14) will reduce the Orowan stress to 181.5 MPa and 169.7 MPa, respectively, and choosing f=0.10 and r=120 nm will lead to 128.8 MPa.

Despite the above estimates, the Orowan bypass stress is higher than the stress level conducted in the creep tests, raising the question on whether this stress level is ever reached in reality. It should be emphasized that deformation at elevated temperatures are controlled by thermally activated processes, whereas the applied stress biases the activation energy barrier. The Orowan stress and other strengthening mechanisms contribute to the reference stress and thus could be higher than the applied stress. For example, for nanosized precipitation strengthened Al-Sc alloy, Marquis et al. [70] estimated an Orowan stress of about 200 MPa while their creep tests are at stress levels less than 100 MPa. This is similar to our L1₂ precipitates in Al_{0.3}CoCrFeNi alloys tested at 973 K under 75 and 110 MPa.

In the creep specimen of 250 h, both granular L₁₂ and lath-like B₂ phases were observed, as shown in Figs. 5 and 4. Diao et al. [32] studied the strengthening effect of the B2 phase by the in situ neutron experiment. After the yielding point, the matrix started to deform plastically, while the B2 precipitates still deformed elastically, and the majority of the total strain was transferred to precipitates. Since the lath-like B2 phase is significantly large and incoherent with the matrix, as presented in Fig. 6, the dislocation in Al_{0.3}CoCrFeNi can only be blocked and formed a pileup around the B2 phases. Here, the Orowan mechanism of Eqs. (3) and (4) was applied again to account for the strengthening effect of the interaction between the B2 phase and the mobile dislocations. The volume fraction is estimated as 16.3% according to Fig. S4 (b). The radius, r, is determined as the average cylindrical radius of the B2 particles and is in the range of 20-100 nm. The calculated result was presented in Fig. 15. It should be noted that at the late stage, i.e., 250 h, the major B2 precipitates uniformly distribute with multiple dislocations around them in the matrix and dominate the creep deformation.

Although the creep strain rate of $Al_{0.3}$ CoCrFeNi HEA is one order of magnitude lower than CoCrNi, and more orders than other HEA and ferritic alloys, the rupture time, t_r is comparable to CoCrNi, as shown in Fig. 3. This observation appears to violate the Monkman-Grant relationship, i.e., the product of minimum creep rate and rupture time is a constant [71,72]. The relationship originates from the creep-induced growth of intergranular cavities. Therefore, the creep strain rate cannot be adopted as the overall value, but as the deformation field right adjacent to the grain boundaries. As shown in Fig. 4, the late stage of creep deformation witnesses the precipitate-free zone near almost all grain boundaries, so the local creep resistance from precipitates is lost. The matrix shows similar compositions as the Cantor subset alloys, so the rupture lifetime is also similar as shown in Fig. 3(b).

Previous studies proposed that stacking fault energy (SFE) plays an important role in improving tensile or creep strength [33]. In previous studies, Xie et al. [33] found that the CoCrNi has the best creep resistance compared to CoCrFeMnNi, CoCrFeNi, and other ferritic steels. However, the minimum creep rate of $Al_{0.3}$ CoCrFeNi is even lower than that of CoCrNi, as displayed in Fig. 14. Xie et al. reported that the creep

resistance decreased in the order of CoCrNi > CoCrFeMnNi > CoCrFeNi, while the SFE of three alloys follow the order of CoCrNi < CoCrFeMnNi < CoCrFeNi, indicating that the SFE order is opposite to the trend of the creep resistance. Even though the SFE of the Al element is very high at about 80 mJ/m 2 [73], in the present Al_{0.3}CoCrFeNi alloy, the measured SFE is around 6-21 [74] or 30 mJ/m² [75]. The reduction of the SFE of Al_{0.3}CoCrFeNi may be due to the larger atomic-size difference between Al and other elements in the alloy. A low SFE increases the dislocation width between two Shockley partials, which can easily block the full dislocation slip and results in the formation of stacking faults. Such a low SFE is comparable to those of CoCrNi, CoCrFeMnNi, and CoCrFeNi, indicating that the SFE may contribute the comparable strengthening effect to both Al_{0.3}CoCrFeNi and CoCrNi alloys. Additionally, even though TWIP or TRIP are rarely observed in the present work, SFs are frequently found in the deformed Al_{0.3}CoCrFeNi at 973 K, as seen in Fig. S5 (Supplementary). From atomistic simulations and theoretical studies of the interaction between dislocations and SFs, it was found that in most cases SFs hindered the glide of other dislocations on slip planes crossing the SF plane, supporting that SFs play an important role in enhancing strain hardening [76]. A wide fluctuation of the SFE on the glide plane due to local ordering may result in the pinning site with a low SFE [33]. In the crept specimens of CoCrNi, CoCrFeMnNi, and CoCrFeNi, only minor σ precipitates were found at the late stage of creep, presenting an insignificant strengthening effect of creep behavior. In one word, the studied Al_{0.3}CoCrFeNi has the best combination of both solid-solution-strengthening and precipitation strengthening, resulting in superior creep properties.

5. Conclusion

The typical tensile creep behavior of a non-equiatomic Al_{0.3}CoCr-FeNi HEA was investigated in the temperature range of 973 - 1033 K. The primary single FCC solid solution is unstable under continuous loading and long durations at elevated temperatures and will decompose into Cr-rich, L12, and lath-like B2 phases in the FCC matrix. The applied tensile stress suppresses the formation of the B2 phase due to its large contractive lattice mismatch from the matrix, thus leading to the appearance of many coherent L12 particles that enhance the creep performance. Intensive dislocation loops, accumulative dislocation tangles, and stacking faults were observed in the crept samples. The stress exponent and activation energy were determined to be 3-6.53 and 390–548.2 kJ⋅mol⁻¹, respectively. Combined with the TEM analysis, the creep deformation is suggested to be dominated by the L12 particledislocation and dislocation-glide at 973 K at the early stage. While with creep proceeding to the late stage, increasing B2 precipitates are produced and replaced L12 as the main obstacle for the mobile dislocations. At a higher temperature of 1033 K, the dislocation glide mechanism is maintained. Compared with other conventional alloys and HEAs, a large reduction of the minimum creep rate, the high-stress exponent, and activation energy is found in the Al_{0.3}CoCrFeNi HEA, indicating a significant improvement in high-temperature properties. This is due to their significant precipitate strengthening and low stacking fault energy of the matrix. This stress-selected precipitation process (i.e., L12 over B2) provides a new strategy for our future design of creepresistant materials.

Data availability

Data contained in this paper are available upon request to the corresponding author.

Declaration of Competing Interest

The authors declare that they have no known competing financial interests or personal relationships that could have appeared to influence the work reported in this paper.

Acknowledgments

SC acknowledges the financial support from the National Natural Science Foundation of China (No. 52001271). YT acknowledges the financial support from the Taishan Scholars Program of Shandong Province (tsqn202103052), and the Top Discipline in Materials Science of Shandong Province. FM appreciates the support from the Natural Science Foundation of Shandong Province (ZR2021QE110). PKL appreciates the support from the National Science Foundation (DMR-1611180 and 1809640) and the US Army Research Office (W911NF-13-1-0438 and W911NF-19-2-0049). APT research was supported by the Center for Nanophase Materials Sciences (CNMS), which is a US Department of Energy, Office of Science User Facility at Oak Ridge National Laboratory. TY is grateful for the financial support from the National Natural Science Foundation of China (11905057, 11935004, and 12175059). The authors would like to thank James Burns and Wei Guo for their assistance in performing APT sample preparation and running the APT experiments. The authors are grateful to the anonymous reviewers for improving the quality and clarify of this work.

Supplementary materials

Supplementary material associated with this article can be found, in the online version, at doi:10.1016/j.actamat.2022.118600.

References

- T. Tanuma, Advances in Steam Turbines for Modern Power Plants, Elsevier Science, 2017.
- [2] B. Cantor, I.T.H. Chang, P. Knight, A.J.B. Vincent, Microstructural development in equiatomic multicomponent alloys, Mater. Sci. Eng. 375–377 (2004) 213–218.
- [3] Y. Zhang, T.T. Zuo, Z. Tang, M.C. Gao, K.A. Dahmen, P.K. Liaw, Z.P. Lu, Microstructures and properties of high-entropy, Prog. Mater. Sci. 61 (2014) 1–93.
- [4] W.D. Li, D. Xie, D.Y. Li, Y. Zhang, Y.F. Gao, P.K. Liaw, Mechanical behavior of highentropy alloys, Prog. Mater. Sci. 118 (2021), 100777.
- [5] D.B. Miracle, O.N. Senkov, A critical review of high entropy alloys and related concepts, Acta Mater. 122 (2017) 448–511.
- [6] B. Gludovatz, A. Hohenwarter, D. Catoor, E.H. Chang, E.P. George, R.O. Ritchie, A fracture-resistant high-entropy alloy for cryogenic applications, Science 345 (6201) (2014) 1153–1158.
- [7] Q.S. Song, L.X. Zhang, R. Feng, Q.H. Lu, K. An, A.C. Chuang, J.D. Poplawsky, P. K. Liaw, L. Lu, Gradient cell–structured high-entropy alloy with exceptional strength and ductility, Science 374 (2021) 984–989.
- [8] P.J. Shi, R.G. Li, Y. Li, Y.B. Zhong, W.L. Ren, Z. Shen, T.X. Zheng, J.C. Peng, X. Liang, P.F. Hu, N. Min, Y. Zhang, Y. Ren, P.K. Liaw, D. Raabe, Y.D. Wang, Hierarchical crack buffering triples ductility in eutectic herringbone high-entropy alloys, Science 373 (2021) 912–918.
- [9] W.D. Li, P.K. Liaw, Y.F. Gao, Fracture resistance of high entropy alloys: a review, Intermetallics 99 (2018) 69–83.
- [10] E.P. George, D. Raabe, R.O. Ritchie, High-entropy alloys, Nat. Rev. Mater. 4 (8) (2019) 515–534.
- [11] Z. Li, S. Zhao, R.O. Ritchie, M.A. Meyers, Mechanical properties of high-entropy alloys with emphasis on face-centered cubic alloys, Prog. Mater. Sci. 102 (2019) 296–345.
- [12] P. Sathiyamoorthi, H.S. Kim, High-entropy alloys with heterogeneous microstructure: processing and mechanical properties, Prog. Mater. Sci. 123 (2020), 100709.
- [13] W.R. Wang, W.L. Wang, S.C. Wang, Y.C. Tsai, C.H. Lai, J.W. Yeh, Effects of Al addition on the microstructure and mechanical property of Al_xCoCrFeNi highentropy alloys, Intermetallics 26 (2012) 44–51.
- [14] B. Gwalani, V. Soni, D. Choudhuri, M. Lee, J.Y. Hwang, S.J. Nam, H. Ryu, S. H. Hong, R. Banerjee, Stability of ordered L1₂ and B2 precipitates in face centered cubic based high entropy alloys Al_{0.3}CoFeCrNi and Al_{0.3}CuFeCrNi₂, Scr. Mater. 123 (2016) 130–134.
- [15] T. Yang, Z. Tang, X. Xie, R. Carroll, G. Wang, Y. Wang, K.A. Dahmen, P.K. Liaw, Y. Zhang, Deformation mechanisms of Al_{0.1}CoCrFeNi at elevated temperatures, Mater. Sci. Eng. A 684 (2016) 552–558.
- [16] D. Choudhuri, B. Gwalani, S. Gorsse, M. Komarasamy, S.A. Mantri, S.G. Srinivasan, R.S. Mishra, R. Banerjee, Enhancing strength and strain hardenability via deformation twinning in fcc-based high entropy alloys reinforced with intermetallic compounds, Acta Mater. 165 (2019) 420–430.
- [17] B. Gwalani, S. Gorsse, D. Choudhuri, Y. Zheng, R.S. Mishra, R. Banerjee, Tensile yield strength of a single bulk Al_{0.3}CoCrFeNi high entropy alloy can be tuned from 160 MPa to 1800 MPa, Scr. Mater. 162 (2019) 18–23.
- [18] D. Xie, R. Feng, P.K. Liaw, H. Bei, Y. Gao, Tensile creep behavior of an equiatomic CoCrNi medium entropy alloy, Intermetallics 121 (2020), 114556.

- [19] W. Woo, E.W. Huang, J.W. Yeh, H. Choo, C. Lee, S.Y. Tu, *In-situ* neutron diffraction studies on high-temperature deformation behavior in a CoCrFeMnNi high entropy alloy, Intermetallics 62 (2015) 1–6.
- [20] Y.B. Kang, K.H. Lee, S.I. Hong, Creep behaviors of CrMnFeCoNi high entropy alloy at intermediate temperatures, Key Eng. Mater. 737 (2017) 21–26.
- [21] C. Cao, J. Fu, T. Tong, Y. Hao, P. Gu, H. Hao, L. Peng, Intermediate-temperature creep deformation and microstructural evolution of an equiatomic FCC-structured CoCrFeNiMn high-entropy alloy, Entropy 20 (12) (2018) 960.
- [22] M. Zhang, E.P. George, J.C. Gibeling, Elevated-temperature deformation mechanisms in a CrMnFeCoNi high-entropy alloy, Acta Mater. 218 (2021), 117181.
- [23] M. Zhang, E.P. George, J.C. Gibeling, Tensile creep properties of a CrMnFeCoNi high-entropy alloy, Scr. Mater. 194 (2021), 113633.
- [24] Y.B. Kang, S.H. Shim, K.H. Lee, S.I. Hong, Dislocation creep behavior of CoCrFeMnNi high entropy alloy at intermediate temperatures, Mater. Res. Lett. 6 (12) (2018) 689–695.
- [25] S. Yoshida, T. Ikeuchi, T. Bhattacharjee, Y. Bai, A. Shibata, N. Tsuji, Effect of elemental combination on friction stress and Hall-Petch relationship in facecentered cubic high /medium entropy alloys, Acta Mater. 171 (2019) 201–215.
- [26] F. Dobeš, H. Hadraba, Z. Chlup, A. Dlouhý, M. Vilémová, J. Matejíček, Compressive creep behavior of an oxide-dispersion-strengthened CoCrFeMnNi high-entropy alloy, Mater. Sci. Eng. A 732 (2018) 99–104.
- [27] W.J. Kim, H.T. Jeong, H.K. Park, K. Park, T.W. Na, E. Choi, The effect of Al to high-temperature deformation mechanisms and processing maps of Al_{0.5}CoCrFeMnNi high entropy alloy, J. Alloy. Compd. 802 (2019) 152–165.
- [28] M.G. Jo, J.Y. Suh, M.Y. Kim, H.J. Kim, W.S. Jung, D.I. Kim, H.N. Han, High temperature tensile and creep properties of CrMnFeCoNi and CrFeCoNi highentropy alloys, Mater. Sci. Eng. A 838 (2022), 142748.
- [29] Y. Tong, J.C. Qiao, Y. Yao, The constitutive model and threshold stress for characterizing the deformation mechanism of Al_{0.3}CoCrFeNi high entropy alloy, Mater. Sci. Eng. A 730 (2018) 137–146.
- [30] W. Guo, D.A. Garfinkel, J.D. Tucker, D. Haley, G.A. Young, J.D. Poplawsky, An atom probe perspective on phase separation and precipitation in duplex stainless steels, Nanotechnology 27 (25) (2016), 254004.
- [31] K. Thompson, D. Lawrence, D.J. Larson, J.D. Olson, T.F. Kelly, B. Gorman, In situ site-specific specimen preparation for atom probe tomography, Ultramicroscopy 107 (2–3) (2007) 131–139.
- [32] H. Diao, D. Ma, R. Feng, T. Liu, C. Pu, C. Zhang, W. Guo, J.D. Poplawsky, Y. Gao, P. K. Liaw, Novel NiAl-strengthened high entropy alloys with balanced tensile strength and ductility, Mater. Sci. Eng. A 742 (2019) 636–647.
- [33] D. Xie, R. Feng, P.K. Liaw, H. Bei, Y. Gao, Long-term tensile creep behavior of a family of FCC-structured multi-component equiatomic solid solution alloys, Scr. Mater. 212 (2022), 114556.
- [34] Z. Zhu, T. Yang, R. Shi, X. Quan, J. Zhang, R. Qiu, B. Song, Q. Liu, The effects of annealing at different temperatures on microstructure and mechanical properties of cold-rolled Al_{0.3}CoCrFeNi high-entropy alloy, Metals 11 (6) (2021) 940 (Basel).
- [35] C.M. Cao, J. Xu, W. Tong, Y.X. Hao, P. Gu, L.M. Peng, Creep behaviour and microstructural evolution of Al_xCrMnFeCoNi high-entropy alloys, Mater. Sci. Technol. 35 (10) (2019) 1283–1290.
- [36] K.H. Lee, S.K. Hong, S.I. Hong, Precipitation and decomposition in CoCrFeMnNi high entropy alloy at intermediate temperatures under creep conditions, Materialia 8 (2019), 100445.
- [37] B. Schuh, F. Mendez-Martin, B. Völker, E.P. George, H. Clemens, R. Pippan, A. Hohenwarter, Mechanical properties, microstructure and thermal stability of a nanocrystalline CoCrFeMnNi high-entropy alloy after severe plastic deformation, Acta Mater. 96 (2015) 258–268.
- [38] E.J. Pickering, R. Muñoz-Moreno, H.J. Stone, N.G. Jones, Precipitation in the equiatomic high-entropy alloy CrMnFeCoNi, Scr. Mater. 113 (2016) 106–109.
- [39] B. Gwalani, S. Gorsse, D. Choudhuri, M. Styles, Y. Zheng, R.S. Mishra, R. Banerjee, Modifying transformation pathways in high entropy alloys or complex concentrated alloys via thermo-mechanical processing, Acta Mater. 153 (2018) 169–185
- [40] H.Y. Yasuda, H. Miyamoto, K. Cho, T. Nagase, Formation of ultrafine-grained microstructure in Al 0.3 CoCrFeNi high entropy alloys with grain boundary precipitates, Mater. Lett. 199 (2017) 120–123.
- [41] T.T. Shun, Y.C. Du, Microstructure and tensile behaviors of FCC Al_{0.3}CoCrFeNi high entropy alloy, J. Alloy. Compd. 479 (1–2) (2009) 157–160.
- [42] J.C. Rao, H.Y. Diao, V. Ocelík, D. Vainchtein, C. Zhang, C. Kuo, Z. Tang, W. Guo, J. D. Poplawsky, Y. Zhou, P.K. Liaw, J.T.M. De Hosson, Secondary phases in Al_xCoCrFeNi high-entropy alloys: an in-situ TEM heating study and thermodynamic appraisal, Acta Mater. (2017) 206–220.
- [43] Q. Tang, Y. Huang, H. Cheng, X. Liao, T.G. Langdon, P. Dai, The effect of grain size on the annealing-induced phase transformation in an Al_{0.3}CoCrFeNi high entropy alloy, Mater. Des. 105 (2016) 381–385.
- [44] X. Gao, Y. Lu, B. Zhang, N. Liang, G. Wu, G. Sha, J. Liu, Y. Zhao, Microstructural origins of high strength and high ductility in an AlCoCrFeNi_{2.1} eutectic highentropy alloy, Acta Mater. 141 (2017) 59–66.
- [45] H.M. Tawancy, A. Ul-Hamid, N.M. Abbas, Practical Engineering Failure Analysis, CRC Press, 2004, p. 616.
- [46] C.R. Reynolds, Z. Herl, N.A. Ley, D. Choudhuri, J.T. Lloyd, M.L. Young, Comparing CALPHAD predictions with high energy synchrotron radiation X-ray diffraction measurements during in situ annealing of Al_{0.3}CoCrFeNi high entropy alloy, Materialia 12 (2020), 100784.
- [47] S. Dasari, A. Sarkar, A. Sharma, B. Gwalani, D. Choudhuri, V. Soni, S. Manda, I. Samajdar, R. Banerjee, Recovery of cold-worked Al_{0.3}CoCrFeNi complex

- concentrated alloy through twinning assisted B2 precipitation, Acta Mater. 202 (2021) 448–462.
- [48] S. Dasari, A. Jagetia, Y.J. Chang, V. Soni, B. Gwalani, S. Gorsse, A.C. Yeh, R. Banerjee, Engineering multi-scale B2 precipitation in a heterogeneous FCC based microstructure to enhance the mechanical properties of a Al_{0.5}Co_{1.5}CrFeNi_{1.5} high entropy alloy, J. Alloy. Compd. 830 (2020), 154707.
- [49] E.A. Anber, A.C. Lang, E.A. Lass, P.K. Suri, J.L. Hart, D.S. D'Antuono, H. Diao, R. Feng, R. Doherty, P.K. Liaw, M.L. Taheri, Insight into the kinetic stabilization of Al_{0.3}CoCrFeNi high-entropy alloys, Materialia 14 (2020), 100872.
- [50] S.H. Sun, Y. Koizumi, S. Kurosu, Y.P. Li, A. Chiba, Phase and grain size inhomogeneity and their influences on creep behavior of Co-Cr-Mo alloy additive manufactured by electron beam melting, Acta Mater. 86 (2015) 305–318.
- [51] A.K. Mukherjee, J.E. Bird, J.E. Dorn, Experimental Correlations for High Temperature Creep, 1968.
- [52] J.Y. He, C. Zhu, D.Q. Zhou, W.H. Liu, T.G. Nieh, Z.P. Lu, Steady state flow of the FeCoNiCrMn high entropy alloy at elevated temperatures, Intermetallics 55 (2014) 9-14
- [53] H.T. Jeong, H.K. Park, K. Park, T.W. Na, W.J. Kim, High-temperature deformation mechanisms and processing maps of equiatomic CoCrFeMnNi high-entropy alloy, Mater. Sci. Eng. A 756 (2019) 528–537.
- [54] H.T. Jeong, H.K. Park, H.S. Kang, W.J. Kim, Operation of solute-drag creep in an AlCoCrFeMnNi high-entropy alloy and enhanced hot workability, J. Alloy. Compd. 824 (2020), 153829.
- [55] H.T. Jeong, H.K. Park, W.J. Kim, Dynamic recrystallization and hot deformation mechanisms of a eutectic Al_{0.7}CoCrFeMnNi high-entropy alloy, J. Alloy. Compd. 871 (2021), 159488.
- [56] T. Cao, J. Shang, J. Zhao, C. Cheng, R. Wang, H. Wang, The influence of Al elements on the structure and the creep behavior of Al_xCoCrFeNi high entropy alloys, Mater. Lett. 164 (2016) 344–347.
- [57] F. Dobeš, P. Dymáček, M. Hasegawa, M. Iwashita, High-temperature creep of a CoNiCrAlY bond coat alloy, Mater. Sci. Eng. A 759 (2019) 272–277.
- [58] S. Haas, A.M. Manzoni, M. Holzinger, U. Glatzel, Influence of high melting elements on microstructure, tensile strength and creep resistance of the compositionally complex alloy Al₁₀Co₂₅Cr₈Fe₁₅Ni₃₆Ti₆, Mater. Chem. Phys. 274 (2021), 125163.
- [59] C. Zakine, C. Prioul, D. François, Creep behavior of ODS steels, Mater. Sci. Eng. A 219 (1996) 102–108.
- [60] J.D. Whittenberger, Creep and tensile properties of several oxide dispersion strengthened nickel base alloys, Metall. Trans. A. 8 (1977) 1155–1163.
- [61] T. Howson, J. Stulga, J. Tien, Creep and stress rupture of oxide dispersion strengthened mechanically alloyed Inconel alloy MA 754, Metall. Trans. A. 11 (1980) 1599–1607.
- [62] G. Song, Z. Sun, L. Li, B. Clausen, S.Y. Zhang, Y. Gao, P.K. Liaw, High temperature deformation mechanism in hierarchical and single precipitate strengthened ferritic alloys by in situ neutron diffraction studies, Sci. Rep. 7 (2017) 45965.
- [63] H. Peng, L. Hu, L. Li, J. Gao, Q. Zhang, On the correlation between L1₂ nanoparticles and mechanical properties of (NiCo)_{52+2x}(AlTi)_{4+2x}Fe_{29-4x}Cr₁₅ (x=0-4) high-entropy alloys, J. Alloy. Compd. 817 (2020), 152750.
- [64] J. Joseph, M. Annasamy, S.R. Kada, P.D. Hodgson, M.R. Barnett, D.M. Fabijanic, Optimising the Al and Ti compositional window for the design of γ' (L1₂)strengthened Al-Co-Cr-Fe-Ni-Ti high entropy alloys, Mater. Sci. Eng. A 835 (2022), 142620.
- [65] Y.L. Zhao, T. Yang, Y.R. Li, L. Fan, B. Han, Z.B. Jiao, D. Chen, C.T. Liu, J.J. Kai, Superior high-temperature properties and deformation-induced planar faults in a novel L1₂-strengthened high-entropy alloy, Acta Mater. 188 (2020) 517–527.
- [66] Y. Ma, Q. Wang, B.B. Jiang, C.L. Li, J.M. Hao, X.N. Li, C. Dong, T.G. Nieh, Controlled formation of coherent cuboidal nanoprecipitates in body-centered cubic high-entropy alloys based on Al₂(Ni,Co,Fe,Cr)₁₄ compositions, Acta Mater. 147 (2018) 213–225.
- [67] J.Y. He, H. Wang, H.L. Huang, X.D. Xu, M.W. Chen, Y. Wu, X.J. Liu, T.G. Nieh, K. An, Z.P. Lu, A precipitation-hardened high-entropy alloy with outstanding tensile properties, Acta Mater. 102 (2016) 187–196.
- [68] T. Xiong, S. Zheng, J. Pang, X. Ma, High-strength and high-ductility AlCoCrFeNi_{2.1} eutectic high-entropy alloy achieved via precipitation strengthening in a heterogeneous structure, Scr. Mater. 186 (2020) 336–340.
- [69] G. Laplanche, P. Gaduad, C. Bärsch, K. Demtröder, C. Reinhart, J. Schreuer, E. P. George, Elastic moduli and thermal expansion coefficients of medium-entropy subsystems of the CrMnFeCoNi high-entropy alloy, J. Alloy. Compd. 746 (2018) 244-255.
- [70] E.A. Marquis, D.N. Seidman, D.C. Dunand, Effect of Mg addition on the creep and yield behavior of an Al-Sc alloy, Acta Mater. 51 (2003) 4751–4760.
- [71] W. Zhang, X. Wang, Y. Wang, X. Yu, Y.F. Gao, Z. Feng, Type IV failure in weldment of creep resistant ferritic alloys: II. creep fracture and lifetime prediction, J. Mech. Phys. Solids 134 (2020), 103775.
- [72] W. Zhang, Y.F. Gao, Z.L. Feng, X. Wang, S. Zhang, L. Huang, Z.W. Huang, L. Jiang, Ductility limit diagrams for superplasticity and forging of high temperature polycrystalline materials, Acta Mater. 194 (2020) 378–386.
- [73] Z. Li, S. Zhao, H. Diao, P.K. Liaw, M.A. Meyers, High-velocity deformation of Al_{0.3}CoCrFeNi high-entropy alloy: remarkable resistance to shear failure, Sci. Rep. 7 (2017) 42742.
- [74] X.D. Xu, P. Liu, Z. Tang, A. Hirata, S.X. Song, T.G. Nieh, P.K. Liaw, C.T. Liu, M. W. Chen, Transmission electron microscopy characterization of dislocation

- structure in a face-centered cubic high-entropy alloy ${\rm Al_{0.1}CoCrFeNi}$, Acta Mater. 144 (2018) 107–115.
- [75] J. Liu, C. Chen, Y. Xu, S. Wu, G. Wang, H. Wang, Y. Fang, L. Meng, Deformation twinning behaviors of the low stacking fault energy high-entropy alloy: an *in-situ* TEM study, Scr. Mater. 137 (2017) 9–12.
- [76] Y.Z. Tian, L.J. Zhao, S. Chen, A. Shibata, Z.F. Zhang, N. Tsuji, Significant contribution of stacking faults to the strain hardening behavior of Cu-15%Al alloy with different grain sizes, Sci. Rep. 5 (2015) 16707.